TOPOLOGY OPTIMIZATION USING HYPER RADIAL

BASIS FUNCTION NETWORK

by

ADITYA PRAKASH APTE

Presented to the Faculty of the Graduate School of

The University of Texas at Arlington in Partial Fulfillment

of the Requirements

for the Degree of

DOCTOR OF PHILOSOPHY

THE UNIVERSITY OF TEXAS AT ARLINGTON

December 2009

This work is dedicated to Ajay mama.

Your positive attitude is a great inspiration to one and all

ACKNOWLEDGEMENTS

I would like to acknowledge my parents, brother and Prof. Bo Ping Wang for their constant encouragement, support and guidance. Thanks to the dissertation committee members, relatives and friends for their direct or indirect help.

<div align="right">October 30, 2009</div>

ABSTRACT

TOPOLOGY OPTIMIZATION USING HYPER RADIAL

BASIS FUNCTION NETWORK

Aditya Prakash Apte, PhD

The University of Texas at Arlington, 2009

Supervising Professor: Bo Ping Wang

Topology optimization has been conventionally used in automobile and aerospace industries to produce lightweight structures for minimum compliance or maximum fundamental frequency. Today, topology optimization finds application in solving diverse types of problems ranging from medicine to consumer products. Popular continuum based method SIMP fails to provide global solution due to too many variables involved. In this work, a novel hyper radial basis function network is presented as topology description function. The proposed approach provides drastic reduction in number of design variables involved in topology optimization. This makes the use of heuristic global solution possible. Parallel processing, reanalysis formulation and automatic selection of optimal volume fraction are proposed to speed up analysis. Application to solve minimum compliance, maximum fundamental frequency, compliant mechanisms and optical medical imaging problems are presented. The proposed approach can be easily incorporated with legacy software. The design process is made efficient by speeding up analysis and decreasing the need for human interpretation.

TABLE OF CONTENTS

vii

LIST OF ILLUSTRATIONS

xi

LIST OF TABLES

CHAPTER 1

INTRODUCTION

1.1 Historical Perspective on Structural Optimization

"Optimization is intrinsically tied to our desire to excel, whether we are an athlete, artist or engineer" [1]. Optimization has therefore naturally manifested into improved performance of structural components and savings in costs. This section provides a brief overview of progression of Structural optimization over the last five decades. Structural optimization dates to the work of Maxwell (1869) and Mitchell (1904). Structural optimization in 1950's was mostly random search. Shanley's work (1952) used analytical methods. 1960 saw a groundbreaking paper by Schmit which ushered modern, computer based era of structural optimization. In his 1981 review of Structural Synthesis development, Schmit credits a paper by Klein (1955) for providing some key ideas. 1960s saw a great deal of research in structural optimization, dealing mainly with member sizing of trusses, frames and shell structures. Sequential Linear Programming (Kelly, 1960) (SLP), Sequential Unconstrained Minimization Techniques (Fiacco and McCormick, 1968) (SUMT) and Feasible Directions methods (Zoutendijk, 1960) came forth. Finite difference gradients were mostly used. Analytical Gradient calculation by Fox was provided in 1965. Structural Optimization could handle only small number of design variables (about 50). As a result, Structural Optimization almost died as it was considered computationally too expensive to be a usable design tool (Gallatly, Berke and Gibson, 1971). 1970's saw efforts to make Structural Optimization more practical by allowing more number of design variables and efficient computational methods. Optimality criteria offered the ability to deal with large numbers of design variables but with a limited number of constraints and without the generality of numerical optimization methods. Approximation Concepts were developed in Numerical Optimization (Schmit and Farshi, 1974). These methods were based on the concept of creating

1

approximations using the underlying physics to allow for large moves and this reduced the number of detailed finite element analyses from well over 100 to the order of ten. Other notable works in the 1970's included Augmented Lagrange Multiplier (Rockefellar in 1973), Generalized Reduced Gradient (Gabriel and Ragsdell, 1977) and Response Surface Methods (Vanderplaats, 1979). 1980's and beyond can be characterized as a period of refinement. Random search methods gave way to Genetic Search (Hajela, 1990), Simulated Annealing (Nemhauser and Wolsey, 1988), Particle Swarming (James Kennedy and Russell C. Eberhart, 1995), Ant Colony Optimization (Marco Dorigo, 1992), Differential Evolution (Price and Storn,
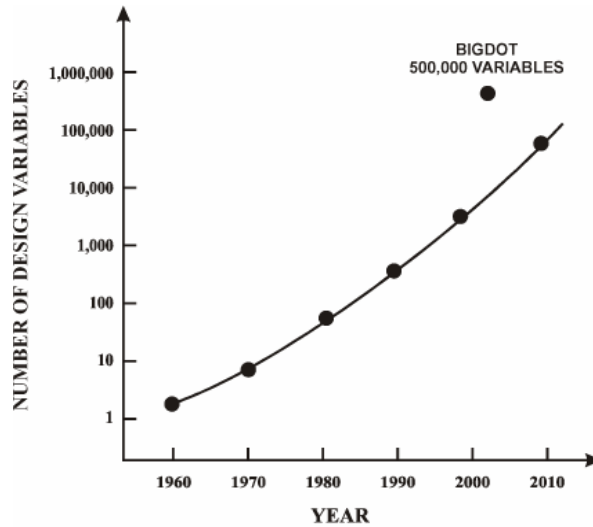
Figure 1.1 Number of Design Variables that can be optimized grew
exponentially (Vanderplaats 2006)

1995), DIRECT (D. R. Jones, C. D. Perttunen and B. E. Stuckman, 1999) and Deterministic global search methods. Sequential Unconstrained Minimization Techniques focused on interior point methods based on the Kuhn-Tucker conditions (Hagar, et al, 1994). An exterior penalty function method was developed for solution of very large scale continuous and discrete variable problems (Vanderplaats, 2004b). Second generation approximations were created using force approximations (Bofang and Zhanmei, 1981 and Vanderplaats and Selajegheh, 1989) instead of the earlier stress approximations. Similarly, Releigh quotient approximations were created for

2

eigenvalue constraints (Canfield, 1990). These new approximations expanded the element types to shell and frame elements among others. Importantly, for such elements as frames it was now possible to treat the physical dimensions as design variables and section properties as intermediate variables so that the designer could now deal with the actual variables of interest. The number of design variables that can be optimized grew exponentially as depicted in Fig. 1 [Vanderplaats]. This led to formulation and solution of sophisticated optimization problems during concept design phase; like topology optimization. Next section describes various categories of structural optimization problems.

<center>1.2 Categories of Structural Optimization</center>

Structural Optimization can be broadly classified into Sizing, Material, Shape and Topology optimization. A good overview with examples has been provided in [Ole Sigmund] and reproduced as follows.

1.2.1 Sizing Optimization

A simple sizing-optimization problem is shown in Fig. 1.2. In the sizing-optimization problem, the layout of the structure is prescribed; in this case, it is a truss structure consisting of 31 truss elements. The cross-sectional area of each element is a design variable. The truss structure is optimized by modifying the areas of the individual truss elements that maximize the stiffness of the truss structure for a given total weight. Sizing optimization is the simplest way of doing structural optimization.

Figure 1.2 Example demonstrating Sizing Optimization (Sigmund [2])

1.2.2 Material Optimization

A simple material-optimization problem is shown in Fig. 1.3. Instead of building the beam as a truss structure, it can be built as a layered fiber-composite. The goal here is to find

<center>3</center>

the material composition that optimizes the stiffness of the beam. In the beam design case, the design variables are the orientations and thicknesses of the individual layers of the composite as shown figure.
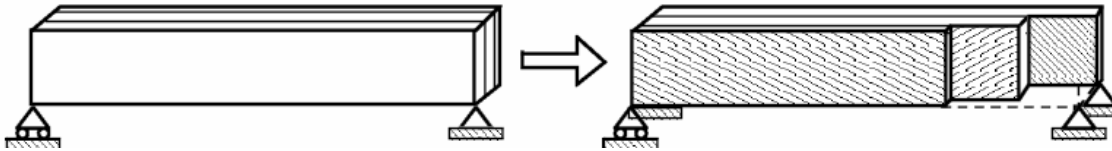
Figure 1.3 Example demonstrating Material Optimization (Sigmund [2])

1.2.3 Shape Optimization

An intuitive way to save weight is to drill circular holes in the structural component. However, circular holes are not structurally efficient. Stress concentrations may be high along the edges of the holes and may cause the structure to break when loaded. The structure may be improved using *shape optimization*. In this case, the design variables are parameters that change the shape of the holes. The procedure is illustrated in figure 1.4.
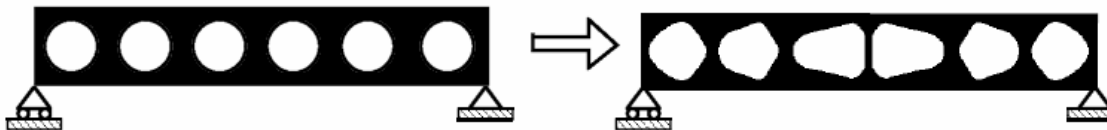
Figure 1.4 Example demonstrating Shape Optimization (Sigmund [2])

1.2.4 Topology Optimization

Given a design volume filled with material, the objective of Topology Optimization is to find the stiffest structure (or a structure fulfilling desired mechanical function) using a specified fraction of the material. This is a powerful tool for defining an initial structure for later refinement using shape and sizing optimization. An example of structural layout produced by topology optimization is shown in figure 1.5.

4
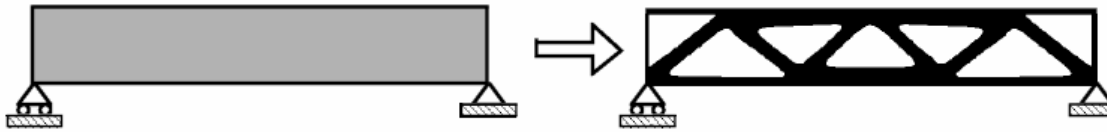
Figure 1.5 Example demonstrating Material Optimization (Sigmund [2])

1.3 Historical Perspective on Topology Optimization

A good review on history and advances in topology optimization was published by Vanderplaats [1], Sigmund [2], Rozvany [3] and Eschenauer and Niels Olhoff [4] and. Some of the highlights have been reproduced here for the ease of reference. Topology Optimization (though not formally referred to as such) dates back to the work of Mitchell (1904) where he presented minimum weight layout of truss structure. Rozvany (1972) and Prager and Rozvany (1977) extended the idea to beam systems. Basic Idea of Continuum based topology optimization was presented by Rossow and Taylor in 1973. Thus, the design region for topology optimization can be represented using discrete [5] (truss/frame) or continuum [4,6] (triangular, quadrilateral, cubic etc) elements. In discrete or ground structure approach the number, position and connectivity between members of structure is optimized. In topology optimization of continuum structures, the shape of external as well as internal boundaries and the number of inner holes are optimized simultaneously with respect to a predefined design objective (Eschenauer and Olhoff, 2001 [4]). Table 1.3.1 (Jasbir S. Arora et al [7]) gives a comparison between the two approaches.

Table 1.1 Comparison between ground structure and continuum based approaches [7]

	Ground Structure	Continuum
Computation Cost	Single analysis cost trivial, but many analyses required	Single analysis cost significant, but few design iterations required
Design Space	Limited	Allows "many" more arrangements of members than discrete
Other considerations	Allows modeling of cross sections	Designs tend to be "unrealistically heavy" due to continuum modeling.

The continuum based approach can be further classified into microstructure (material based) and macrostructure (geometry based). In microstructure approach the finite element grid is fixed and each material is assigned a material density of 0 (void) or 1 (solid). In macrostructure approach the finite element mesh can be deformed during the optimization process to allow for the deformation of geometry. The use of microstructure continuum approach is more common as it spans the entire design region to ensure participation of all sites and same finite element mesh can be reused. The microstructure continuum models traditionally used are homogenization (Bendsoe and Kikuchi [6]), layered microstructure and simultaneous interpolation of material with penalization (SIMP) models (Bendsoe [8]). The SIMP models are preferred due to their simplicity and reduced number of variables (as many as number of finite elements) compared to homogenization and layered microstructure models. SIMP models are used in most of the commercial software. Most of the current research in topology optimization deals with improving the SIMP method for speed and clarity of results. The use of topology description function is one such promising improvement; which this works builds on.

1.4 Rationale for Hyper Radial Basis Function Network as Topology Description Function

The SIMP method computes optimal density of each element and hence there must be as many design variables as the number of finite elements. The number of elements must be sufficient to obtain a correct representation of geometrical features as well as accurate physical

response. The idea of using Topology Description Function (TDF) stems from the fact that the number of elements required in FEA model to represent the geometrical features far exceeds that required to obtain a correct physical response. As such, describing the geometrical features using a TDF instead of the traditional approach leads to a drastic reduction in number of parameters required to describe the geometrical features, assuming that a TDF can be represented by a small number of parameter as compared to the corresponding number of elements required. This permits the use of a coarse mesh (sufficient to obtain correct physical response) in solving the FE analysis problem and results in speed-up of topology optimization while yielding smooth topologies.

The use of TDF has been researched in the past and found to be promising. Modeling material densities as TDF helps get rid of checkerboard patterns as observed by M. Stolpe and K. Svanberg [9]. They used finite element approximation for continuous material distribution in a fixed design space. Important considerations in using TDF are the model representation, where geometry is evolving from an initial state to an optimized one, and the technique used to associate design variables with mesh data. Using constructive solid geometry as a basis for formulating and controlling topology design problem results in robust procedures as observed by V. Kumar *et al* [10] and P.M. Finnigian *et al* [11. De Ruiter, M.J. and Van Keulen [12] used a network of Gaussian basis functions to define topology description function along with the penalization method. The location and widths of these bases were fixed and the only variables were the basis weights. They used as many bases as the number of finite elements. Thus, number of design variables remained the same as those used in SIMP method. S.Y. Wang *et al* [13] used the RBF multiquadric splines to construct the implicit level set function for topology optimization. Level-set methods need to deal with formulating and solving the Hamilton Jacobi equations, which can be challenging. Wavelet [14] is an another way to represent the density function in terms of basis functions that are linked to lengthscales and which are not directly coupled to the finite element mesh of the analysis. Annicchiarico and Cerrolaza [15] used β -

splines and genetic algorithm to solve a specific example of cantilevered beam with circular hole. GY Cui *et al* [16] used Bezier curves for morphological representation of structural geometry and simulated annealing for maximum natural frequency topology design. Though the approaches outlined above sound promising, in general they suffer from (i) difficulties involved with finding the approximation function which correctly represents the material density, (ii) expressing parameters involved in the approximation function as continuous variables for efficient optimization and (iii) gradient-based solution of the optimization problem involved. The parameters used in the methods outlined above to model the material distribution (or geometry) are not intuitive. For example, it is difficult for a user to tweak wavelet parameters to produce a desired effect on the material distribution and so on. On the other hand, hyper radial basis function network (HRBFN) [17, 18] is intuitive and can be made user interactive. After solving the topology design problem; if required, the user can interactively change the location, width, orientation or weight of one or more bases to produce the desired effect on structural topology. The HRBFN parameters are continuous design variables and gradient-based algorithm are developed to solve the topology optimization problem.

8

CHAPTER 2

HYPER RADIAL BASIS FUNCTION NETWORK

2.1 Introduction

Hyper radial basis functions [17, 18] are similar to the radial basis functions commonly used for response surface modeling. Unlike the radial basis, hyper radial basis functions can have different widths in different directions and can be oriented along any direction. The term "hyper" refers to the fact that this basis, and in turn the network, has many widths and orientations. Figure 2.1 shows cross sections of 2D radial basis and hyper radial basis functions with and without orientation.

(a)   (b)   (c)
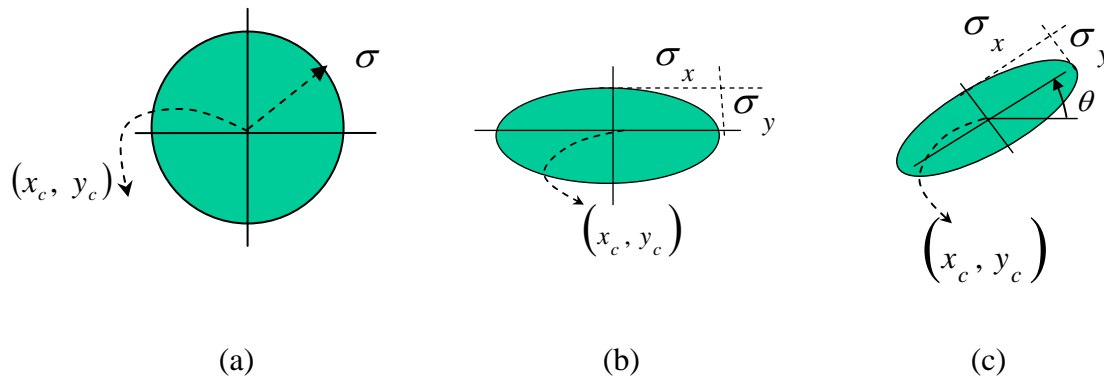
Figure 2.1 Cross sections of 2D (a) Radial Basis function, (b) Hyper Radial Basis with no orientation and (c) Hyper Radial Basis function with orientation

The hyper radial basis is more flexible compared to the regular radial basis. This comes at the cost of introducing nonlinear parameters in the basis, which can be a challenge during optimization. At the same time, there is a drastic reduction in the number of parameters compared to the radial basis network. This is because a single hyper radial basis can used to represent a structural link as opposed to many radial basis functions required to achieve the same. The reduction in number of parameters allows the use of global optimization method,

9

which helps overcome the nonlinearity in design problem including the one introduced by hyper radial basis.

2.2 Mathematical Formulation

2.2 Mathematical Formulation

The parametric model for hyper radial basis function network is represented as

$$f(X) = w_0 + \sum_{i=1}^{r} w_i \phi_i \left(\|X - \mu_i\|, \alpha_i, \theta_i \right) \tag{1}$$

where r is the number of bases, $X \in R^n$ is an input vector, ϕ_i is the basis function, w_i are the weights of the network, $\mu_i = (\mu_{i1}, \mu_{i2} \dots \mu_{in})$ is the location vector of the ith basis, $\alpha_i = (\alpha_{i1}, \alpha_{i2} \dots \alpha_{ip})$ is the orientation vector of the ith basis where p is the number of parameters required to define the orientation of the basis in an n-dimensional space, $\theta_i = (\theta_{i1}, \theta_{i2} \dots \theta_{in})$ is the bandwidth vector of the ith basis and $\| \ \|$ denotes Euclidean norm. The hidden layer for this network represents the parameters $w_i, \mu_i, \alpha_i, \theta_i$ to characterize the material distribution. The output layer represents the material distribution as continuous function of the hidden parameters.

For 2-D design space, $X \in R^2$ i.e. n=2 and p=1. The basis function of the network is chosen to be Gaussian function which can be represented as

$$\phi_i \left(\|X - \mu_i\|, \alpha_i, \theta_i \right) = e^{-g_i^2} \tag{2}$$

where $g_i^2 = \Delta x^T \left[T^T \right] \begin{bmatrix} \dfrac{1}{\theta_{i1}} & 0 \\ 0 & \dfrac{1}{\theta_{i2}} \end{bmatrix} [T] \Delta x$ is always positive.

$$T = \begin{bmatrix} \cos(\alpha_{i1}) & \sin(\alpha_{i1}) \\ -\sin(\alpha_{i1}) & \cos(\alpha_{i1}) \end{bmatrix}, \ \Delta x = \begin{Bmatrix} \bar{\mu}_1 - \mu_{i1} \\ \bar{\mu}_2 - \mu_{i2} \end{Bmatrix}, \ X = (\bar{\mu}_1, \bar{\mu}_2)$$

10

For 3-D design space, $X \in R^3$ i.e. $n=3$ and $p=3$. The Gaussian basis function of this network is be represented by eq. (2) where g^2 is expressed as follows.

$$g_i^2 = \Delta x_i^T \left[T^T \right] \begin{bmatrix} \dfrac{1}{\theta_{i1}} & 0 & 0 \\ 0 & \dfrac{1}{\theta_{i2}} & 0 \\ 0 & 0 & \dfrac{1}{\theta_{i3}} \end{bmatrix} [T] \Delta x_i$$

$$\Delta x_i = \begin{Bmatrix} X - Xc \\ Y - Yc \\ Z - Zc \end{Bmatrix} , \quad X = \left(\overline{\mu}_{i1}, \overline{\mu}_{i2}, \overline{\mu}_{i3} \right), \quad T = T_x T_y T_z$$

$$T_z = \begin{bmatrix} \cos(\alpha_{i1}) & \sin(\alpha_{i1}) & 0 \\ -\sin(\alpha_{i1}) & \cos(\alpha_{i1}) & 0 \\ 0 & 0 & 1 \end{bmatrix},$$

$$T_y = \begin{bmatrix} \cos(\alpha_{i2}) & 0 & \sin(\alpha_{i2}) \\ 0 & 1 & 0 \\ -\sin(\alpha_{i2}) & 0 & \cos(\alpha_{i2}) \end{bmatrix}, T_x = \begin{bmatrix} 1 & 0 & 0 \\ 0 & \cos(\alpha_{i3}) & \sin(\alpha_{i3}) \\ 0 & -\sin(\alpha_{i3}) & \cos(\alpha_{i3}) \end{bmatrix}$$

Thus, the material distribution can be approximated as shown in eq. (3)

$$\rho(X) = \rho(X, w, \mu, \alpha, \theta) = w_0 + \sum_{i=1}^{r} w_i e^{-g_i^2} \tag{3}$$

where w refers to network weights for material distribution (i.e. the basis weights w_i, $i=1$ to r), $\mu = (\mu_1, \mu_2 ... \mu_r)$ refers to the center locations for r bases, $\alpha = (\alpha_1, \alpha_2 ... \alpha_r)$ refers to the angle parameters for r bases, $\theta = (\theta_1, \theta_2 ... \theta_r)$ refers to the bandwidth parameter for r bases. In case of 2-D problems, 6r parameters are required to describe the material distribution or TDF and

11

hence to train the network; whereas in case of 3-D problems, $10r$ parameters are required to describe the material distribution. The next section presents examples of 2D and 3D hyper radial basis functions and the network.

2.3 Examples

Consider a 2-D hyper radial basis with center location (1.5, 1), bandwidth (0.5, 1) and angle (30). Figure 2.2 (a) shows the magnitude and shape of this basis in 2-D space. Figure 2.2 (b) shows the iso-density contour of the basis at a magnitude of 0.05.

(a)   (b)
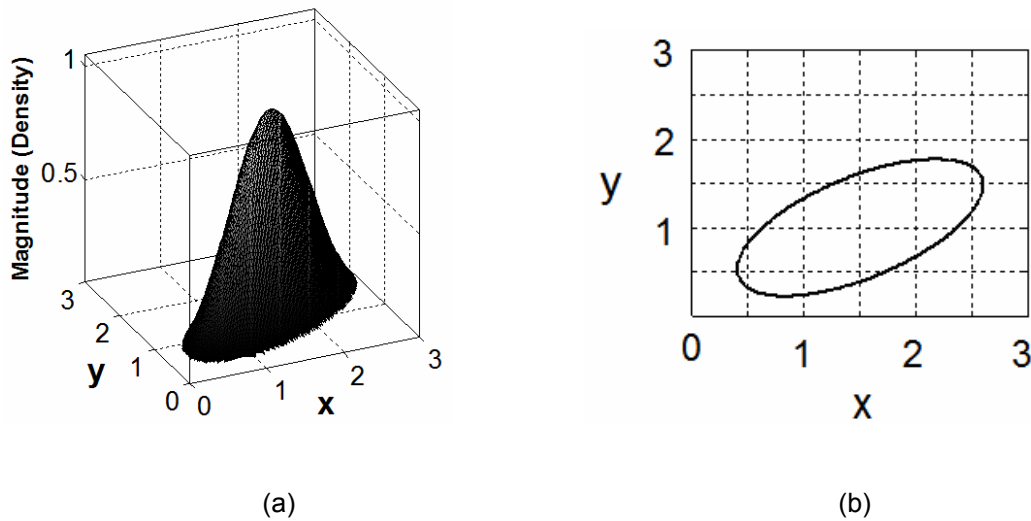
Figure 2.2 (a) Shape and magnitude of 2-D hyper radial basis. (b) Shape (Cross section) of 2-D hyper radial basis at magnitude of 0.05 units

Following is an example of 2-D hyper radial basis network with 2 bases. For the 1st basis let the weight, center location, bandwidth and angle be (1), (1.5, 1), (0.3, 0.1) and (30°) respectively. For the 2nd basis let the weight, center location, bandwidth and angle be (1), (2, 2), (0.25 0.05) and (120°) respectively. Figure 2.3 (a) shows the magnitude and shape of this network in 2-D space. Figure 2.3 (b) shows the iso-density contour of basis at a magnitude of 0.05.

(a)   (b)
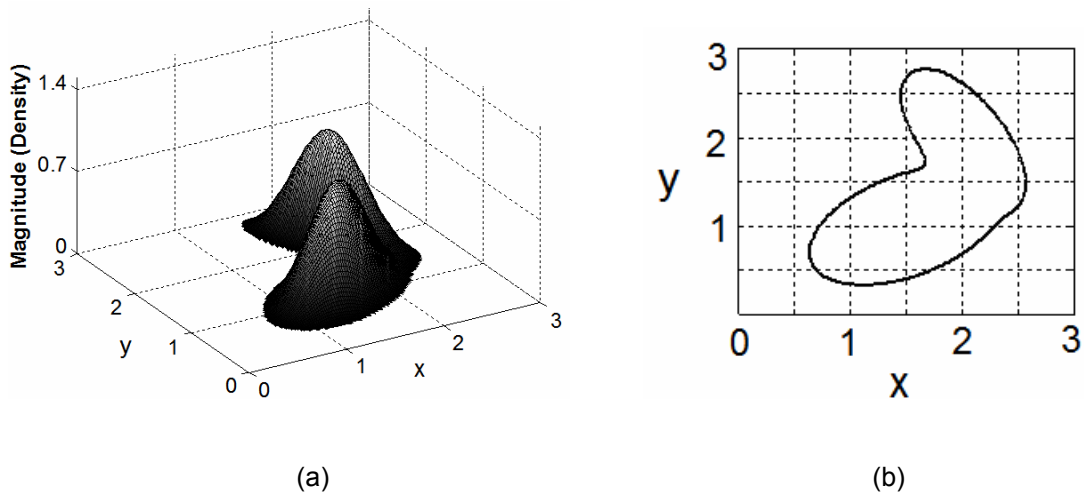
Figure 2.3 (a) Shape and magnitude of 2-D hyper radial basis. (b) Shape (Cross section) of 2-D hyper radial basis at magnitude of 0.05 units

Following are examples of 3-D hyper radial basis function and the network with 2 bases. Figure 2.4 shows the iso-surface for a 3-D hyper radial basis at density level of 0.001 with basis weight 1, center-location (1.5, 1.6, 1.1), bandwidth (0.05, 0.02, 0.5) and angle (30°,
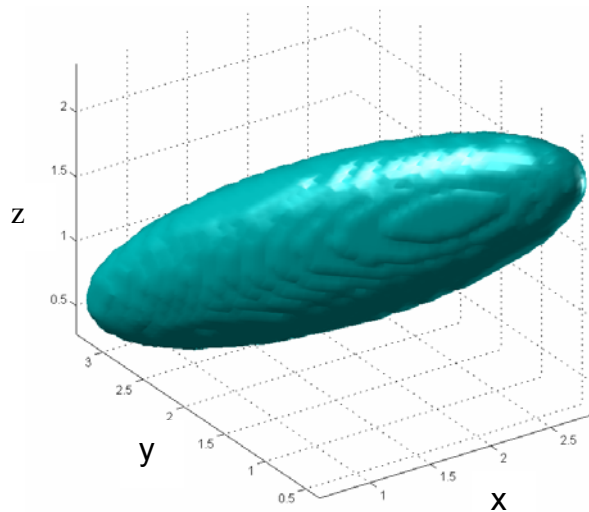
Figure 2.4 Example of 3-D Hyper Radial Basis Function

60°, 20°). Figure 2.5 shows the iso-surfaces for two basis functions (blue and green) of an HRBF network superimposed.
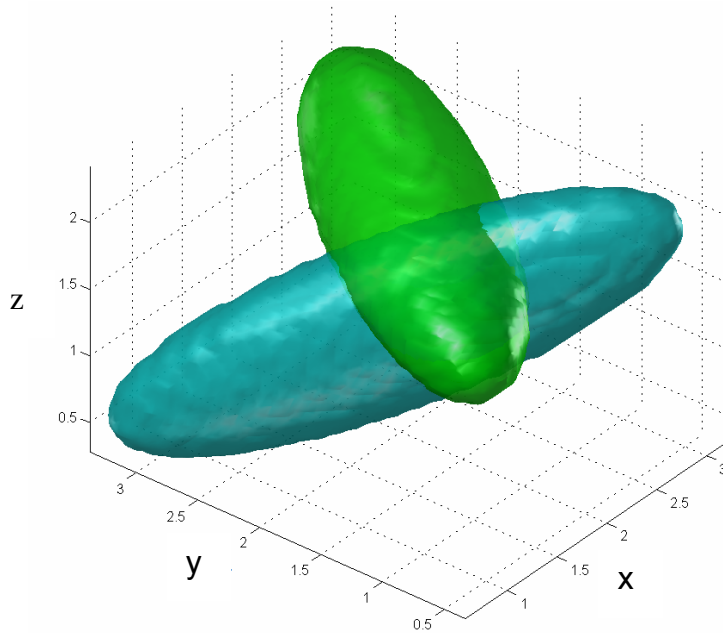
Figure 2.5 Example of 3-D Hyper Radial Basis Function Network

2.3 Conclusion

This chapter presented the mathematical formulation of hyper radial basis function network along with 2D and 3D examples. The examples demonstrate the flexibility of HRNFN in terms magnitude and orientation to model the material distribution in topology optimization and hence make HRBFN an ideal candidate for describing structural topology. Since the parameters governing HRBFN are nonlinear, the optimization problem becomes challenging. The next chapters present algorithm to solve the optimization problem along with application to various topology design problems.

CHAPTER 3

MINIMUM COMPLIANCE AND MAXIMUM FUNDAMENTAL FREQUENCY
TOPOLOGY DESIGN

Topology optimization to design minimum compliance or maximum fundamental frequency structures represents the most commonly solved topology optimization problem. It is applied to problems in automobile, aerospace and commercial products. This chapter presents the problem formulation, solution procedure and examples for the two types of problems. 2-D and 3-D examples are presented for minimum compliance topology design and 2-D examples are presented for maximum fundamental frequency design.

3.1 Minimum Compliance Topology Design

3.1.1 Problem Statement

The optimization problem can be stated as follows

$$\text{Minimize} \quad f = \text{Strain Energy} = \text{Compliance} = u^T K u \qquad (4)$$

where K is the global stiffness matrix of the structure, u is the displacement vector obtained by solving the system of equations

$$K u = P \qquad (5)$$

where P is the vector of global nodal loads and K is assembled from the elemental stiffness matrices as follows.

$$K = \sum_{j=1}^{N_e} \left(\rho_j^{n^*} + \rho_{reg} \right) (K_e)_j \tag{6}$$

where $(K_e)_j$ is the elemental stiffness matrix for the jth element and N_e is the number of elements for finite element analysis. $n^* = 4$ was used in this work. The choice of the value of n^* was based on previous literature and to maintain the positive-definiteness of stiffness matrix. The density ρ_j of an element might become (-) ve during the optimization process due to (-) ve basis weights; but an even power of n^* ensures that stiffness matrix is positive-definite. $\rho_{req} = 10^{-3}$ was used to avoid singularity in stiffness matrix. ρ_j, the density of jth element, is governed by HRBFN as follows

$$\rho_j = \rho_j(Xe_j, Ye_j, Ze_j) = \sum_{i=1}^{r} w_i e^{-g_i^2} \tag{7}$$

where (Xe_j, Ye_j, Ze_j) is the centroid of jth element. Note that the density across each element is assumed constant and evaluated at its centroid. The constraints for this problem are described as follows.

(i) Total material usage should be less than the specified value as represented by eq. (8).

$$\sum_{j=1}^{N_e} \rho_j \le \rho_{req} \tag{8}$$

where ρ_{req} is the total volume of material to be retained. Note that unlike traditional SIMP, there is no upper limit of 1 for elemental pseudo-density. In our experience, this upper limit of 1 makes the material to spill over to unnecessary elements just to satisfy the total fraction material

16

constraint. On the other hand if there is no upper limit on the elemental density, the elements on load path, which are important, get high density values. The material does not spill over to the unnecessary elements since the fraction material constraint gets satisfied from higher density values for the important elements. This makes a priori knowledge of fraction volume or the use of adaptive fraction volume selection algorithms [19] not necessary for the proposed approach. One of the ramifications of not imposing upper bound of 1 on pseudo-density is that the user defined material properties might be rendered useless. The workaround would be to pass the pseudo-density through a sigmoid function or normalization by maximum of all the elemental pseudo densities. Then the stiffness matrix would be scaled by pseudo-densities lying between 0 and 1, whereas the constraints would be computed using the raw (no upper bound) pseudo-densities. This normalization was not implemented in the current work since we were not concerned about the exact value of compliance.

(ii) The problem formulation allows for negative weights for individual basis functions. But the material density at each element, which is a linear combination of contributions from various basis functions, should be non-negative. Equation 9 represents this constraint.

$$\rho_j \geq 0 \text{ for } j = 1 \text{ to } N_e \tag{9}$$

(iii) Bounds for HRBFN parameters are chosen based on the design domain. The bounds for weight parameters range from $w_{Low} = -1$ to $w_{High} = 1$ to allow formation of cavities. Figures 3 and 4 demonstrate the use of negative basis weights in formation of cavities. Two-dimensional cross-sections are presented for the ease of visualization and the same logic holds true for three dimensional geometries. As shown in figure 3.1 (a) four basis functions with positive weights are required to form a cavity as opposed to just two basis functions in figure 3.1 (b).

(a)	(b)
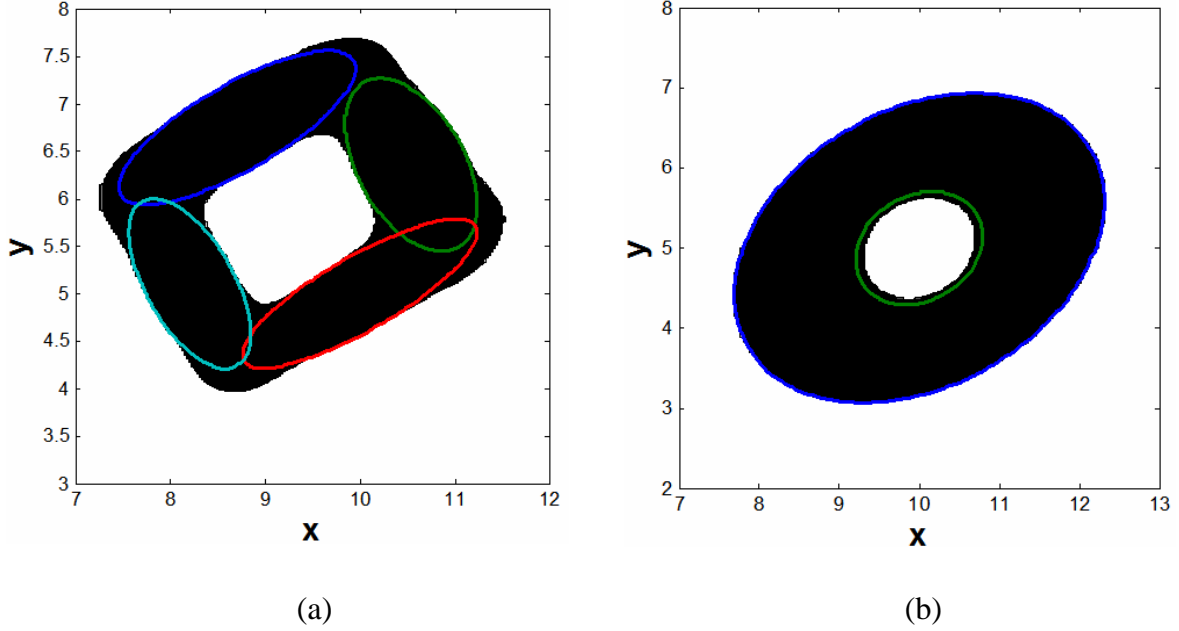
Figure 3.1 (a) Formation of cavity using four basis functions with equal weight of 1, (b) Formation of cavity using two basis functions with weights of 1 and -1.2 for big and small basis respectively

Thus, allowing negative basis-weights significantly increase the flexibility of network to represent intricate geometries. The bounds for location parameter μ are chosen to span the entire design domain. The bounds for bandwidth θ are chosen to be a fraction size of design domain ensuring that a network base is capable of spanning the entire breadth of the design space. The bounds for angle parameters range from $\alpha_{Low} = 0°$, $\alpha_{High} = 180°$ to ensure that the network base can be oriented in any direction.

3.1.2 Sensitivity Analysis

Sensitivity analysis refers to computation of gradients of objective function with respect to the design variables. Analytical sensitivity analysis was performed to speed-up the optimization process. The sensitivity of compliance with respect to an HRBFN parameter $\hbar$ can be computed as follows. Differentiating eq. (4) w.r.t. parameter $\hbar$, we obtain

18

$$\frac{df}{d\hbar} = \frac{d\left(U^T K U\right)}{d\hbar} = 2U^T K \frac{dU}{d\hbar} + U^T \frac{dK}{d\hbar} U \qquad (10)$$

Note that $\hbar = \left(w, \mu, \alpha \ or \ \theta\right)$ for each basis. $\hbar_i$ can be one of the basis parameters $w_i, \mu_{i1}, \mu_{i2}, \mu_{i3}, \theta_{i1}, \theta_{i2}, \theta_{i3}, \alpha_{i1}, \alpha_{i2}, \alpha_{i3}$. The load vector in eq. (5) is independent of design variables. Differentiating eq. (5) and pre-multiplying by U^T, we get

$$U^T K \frac{dU}{d\hbar} = -U^T \frac{dK}{d\hbar} U \qquad (11)$$

Substituting eq. (11) in eq. (10), we obtain the sensitivity of objective f w.r.t. parameter $\hbar$.

$$\frac{df}{d\hbar} = -U^T \frac{dK}{d\hbar} U \qquad (12)$$

$\frac{dK}{d\hbar}$ in eq. (12) can be computed analytically or by using approximate method like finite difference or complex variable method [20, 21]. In this work the analytical sensitivity was implemented and verified with finite difference and complex variable methods. Differentiating eq. (6) w.r.t. one of the parameters for i^{th} basis, we obtain

$$\frac{\partial K}{\partial \hbar_i} = \frac{\partial \sum_{j=1}^{N_e} \left(\rho_j^{n^*} + \rho_{reg}\right)(K_e)_j}{\partial \hbar_i} \qquad (13)$$

Substituting eq. (7) in eq. (13), we obtain

$$\frac{\partial K}{\partial \hbar_i} = \frac{\partial \sum_{j=1}^{N_e} \left(\sum_{i=1}^{r} w_i e^{-g_i^2} \right)^{n^*} (K_e)_j}{\partial \hbar_i}$$ (14)

On further simplifying eq. (14), we obtain

$$\frac{\partial K}{\partial \hbar_i} = \sum_{j=1}^{N_e} \left(\frac{\partial \left(w_i e^{-g_i^2} \right)^{n^*}}{\partial \hbar_i} \right) (K_e)_j$$ (15)

Thus, the sensitivity of compliance to HRBFN parameters can be obtained analytically by substituting eq. (15) in eq. (11).

3.1.3 Solution Procedure

Parameterization of topology using HRBFN drastically reduces the dimension of design space from thousands of variables (equal to the number of finite elements) to a few hundred HRBFN parameters. This permits the use of global optimization techniques since enough sample points can be generated to span the entire design space. In this work, a swarm based global optimization method; Particle Swarm Optimization (PSO) [22, 23] was used to provide the starting point for gradient based algorithm to ensure global optimal solution. Sequential linear programming and perturbations were used to refine the global PSO solution. The final structure was obtained by retaining densies above certain level referred to as the optimal density-level. An automated method to calculate optimal density-level was developed. The optimal density level is selected such that no further reduction in compliance occurs with decrease in cutoff value for density. The flowchart in figure 3.2 briefly describes the design procedure used to design topology. The next sections describe gradient-based algorithm in detail. The details about global optimization algorithm PSO can be obtained from [22, 23].
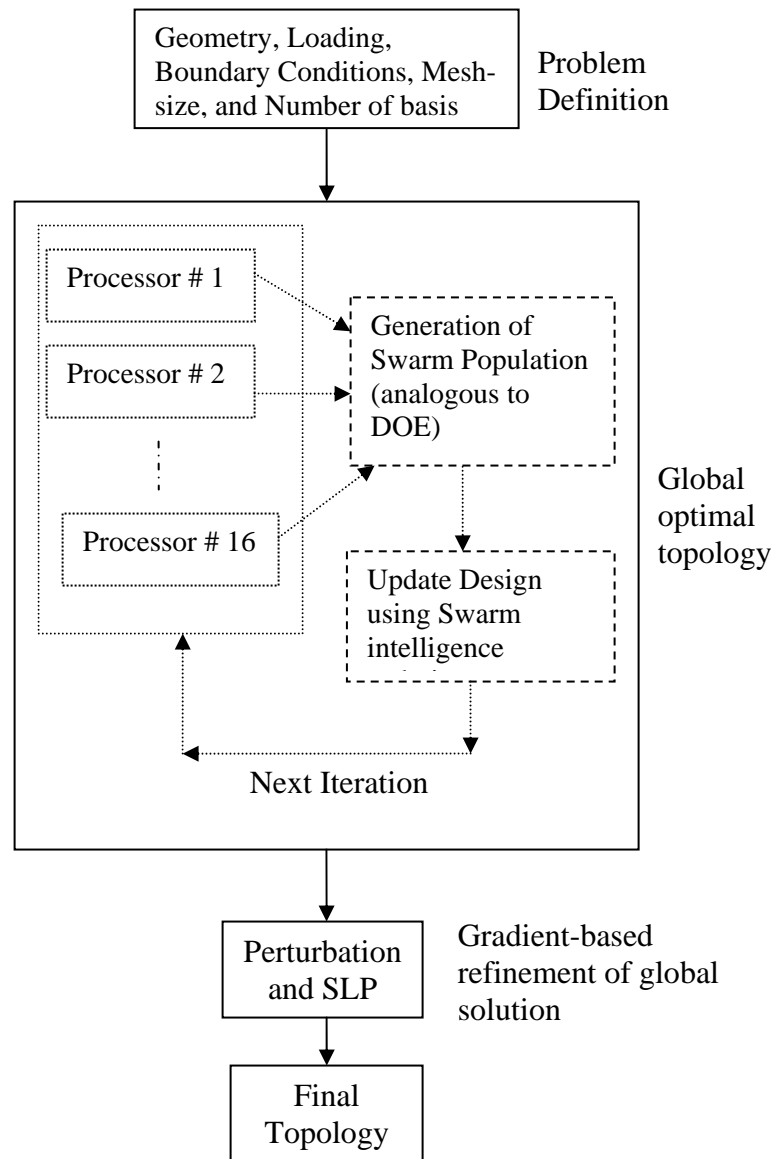
Figure 3.2 Flowchart for Solution Procedure

3.1.3.1 Perturbation algorithm to obtain a minimum compliance design close to the optimal solution.

Figure 3.1.3 briefly describes the perturbation algorithm. The nonlinear design variables - location and angle are perturbed based on the signs of their sensitivities. The nonlinear design variable bandwidth is perturbed based on the sign of difference between its sensitivity and the

median of sensitivities of bandwidths of all the bases. This is because the sensitivity of compliance with respect to the bandwidth is always negative for structures with symmetric (positive definite) stiffness matrices. This is explained in more detail as follows through eq. (10) and (14). Consider the sensitivity of compliance with respect to 1st bandwidth for the ith base (θ_{i1}). Eq. (9) can be rewritten for bandwidth variable as

$$\frac{dC}{d\theta_{i1}} = -\frac{1}{2} U^T \frac{dK}{d\theta_{i1}} U \tag{10}$$

Substituting eq. (6) in eq. (10), we obtain eq. (11) as

$$\frac{dC}{d\theta_{i1}} = -\frac{1}{2} U^T \frac{d\sum_{j=1}^{N_e} \left(\rho_j^{n^*} + \rho_{reg} \right) (K_e)_j}{d\theta_{i1}} U \tag{11}$$

Substituting the density from eq. (3) in eq. (11), we obtain eq. (12) as

$$\frac{dC}{d\theta_{i1}} = -\frac{1}{2} U^T \frac{d\sum_{j=1}^{N_e} \left(\left(\sum_{i=1}^{r} w_i e^{-g_i^2} \right)^{n^*} + \rho_{reg} \right)(K_e)_j}{d\theta_{i1}} U \tag{12}$$

Differentiating eq. (11) with respect to the bandwidth, we obtain the sensitivity in eq. (13)

$$\frac{dC}{d\theta_{i1}} = -\frac{1}{2} U^T \left[\sum_{j=1}^{N_e} \frac{n^* (Xe_j - \mu_{i1})^2 \rho_j^{n^*} (K_e)_j}{\theta_{i1}^2} \right] U \tag{13}$$

Similarly, for 2nd bandwidth of the ith base, we obtain sensitivity as shown in eq. (14).

$$\frac{dC}{d\theta_{i2}} = -\frac{1}{2} U^T \left[\sum_{j=1}^{N_e} \frac{n^* (Ye_j - \mu_{i2})^2 \rho_j^{n^*} (K_e)_j}{\theta_{i2}^2} \right] U \tag{14}$$
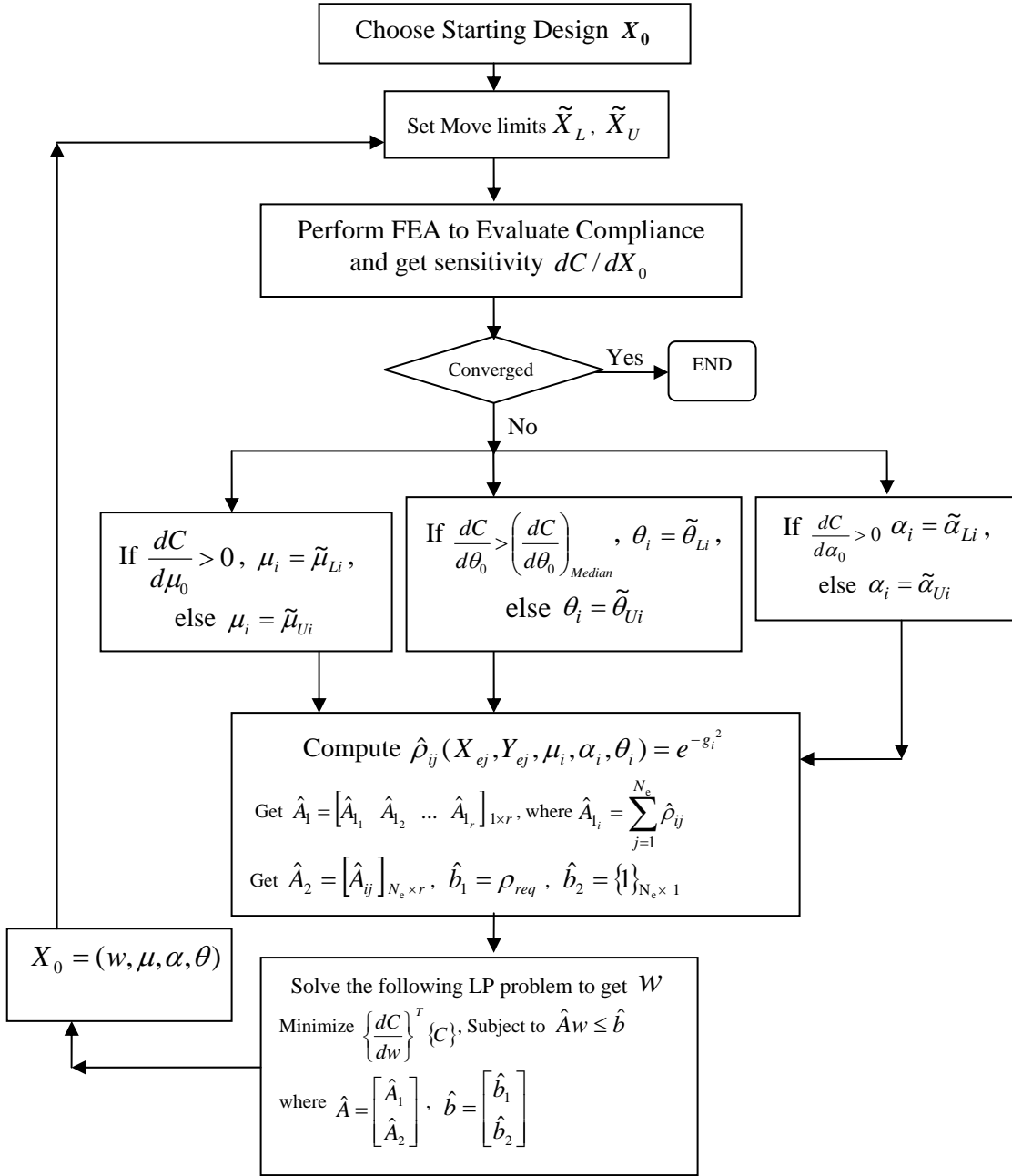
Figure 3.3 Flowchart for Perturbation and SLP algorithm

Note that in eq. (13) and (14), the term in $[\ ]$ is always positive definite. Hence, the sensitivity given by eqs. (13) and (14) is always negative. The linear variable weight is computed using linear programming by imposing the constraints as shown in figure 3.1.3.

3.1.3.2 Sequential linear programming starting from the design yielded by p

This section shows how the topology optimization problem is formulated as linear programming (LP) problem [24]. The topology optimization problem for minimum compliance design can be mathematically stated as shown in eq. (7), (15) and (16).

Minimize $C = \dfrac{1}{2} U^T K U$

Subject to $\displaystyle\sum_{j=1}^{N_e} \rho_j \leq \rho_{req}$ (15)

and $\rho_j \leq 1$ (16)

where $j = 1$ to N_e, N_e is the number of elements in FE analysis model and ρ_{req} is the total volume of material to be retained. The standard form of LP problem is:

Calculate x to minimize $f^T x$ subject to $Ax \leq B$.

Hence, the objective and constraints in our compliance minimization problem should be formulated to be compatible with the LP formulation. The objective function can be reformulated using Taylor's series expansion for compliance by retaining up to 1st order terms as follows.

$$C = C_{0j} + \sum_{i=1}^{N_{dv}} \frac{\partial C}{\partial x_i}\left(x_i - x_{i0}\right)$$ (17)

$$C = C_{0j} - \sum_{i=1}^{N_{dv}} \frac{\partial C}{\partial x_i} x_{i0} + \sum_{i=1}^{N_{dv}} \frac{\partial C}{\partial x_i} x_i$$ (18)

where N_{dv} is the number of design variables. Specifically, N_{dv} = 6r for 2D and N_{dv} = 10r for 3D.

Note that the first two terms in eq. (18) are constant and independent of the new design. Hence, minimizing C in eq. (18) is same as minimizing eq. (19)

$$C = \sum_{i=1}^{N_{dv}} \frac{\partial C}{\partial x_i} x_i \tag{19}$$

In matrix form

$$C = [F]^T \{x\} \tag{20}$$

where $[F] = \dfrac{\partial C}{\partial x}$ is the gradient of compliance evaluated at current design x_0 and has the dimension $N_{dv} \times 1$.

x is a vector of design variables, i.e. the HRBFN parameters and has the dimension $N_{dv} \times 1$.

The constraint eq. (15) can be formulated as follows.

$$\sum_{j=1}^{N_e} \rho_j \leq \rho_{req}$$

Using Taylor's series expansion and retaining only 1st order term,

$$\sum_{j=1}^{N_e} \left(\rho_{0j} + \sum_{i=1}^{N_{dv}} \frac{\partial \rho_j}{\partial x_i} (x_i - x_{i0}) \right) \leq \rho_{req} \tag{21}$$

$$\sum_{j=1}^{N_e} \sum_{i=1}^{N_{dv}} \frac{\partial \rho_j}{\partial x_i} x_i \leq \rho_{req} - \sum_{i=1}^{N_e} \rho_{0j} + \sum_{j=1}^{N_e} \sum_{i=1}^{N_{dv}} \frac{\partial \rho_j}{\partial x_i} x_{i0} \tag{22}$$

In matrix form,

$$A_1 x \leq b_1 \tag{23}$$

where $A_1 = \sum_{j=1}^{N_e} \frac{\partial \rho_j}{\partial x}$ is of the dimension $1 \times N_{dv}$.

x is a vector of design variables, i.e. the HRBFN parameters and has the dimension $N_{dv} \times 1$.

$$b_1 = \rho_{req} - \sum_{j=1}^{N_e} \rho_{0j} + \sum_{j=1}^{N_e} \sum_{i=1}^{N_{dv}} \frac{\partial \rho_j}{\partial x_i} x_{i0} \text{ is of the dimension } 1 \times 1$$

The constraint eq. (16) can be formulated as follows

$$\rho_j \le 1$$

Using Taylor's series expansion and retaining only 1st order term,

$$\rho_{0j} + \sum_{i=1}^{N_{dv}} \frac{\partial \rho_j}{\partial x_i}(x_i - x_{i0}) \le 1 \text{ for } j = 1 \text{ to } N_e \qquad (24)$$

$$\sum_{i=1}^{N_{dv}} \frac{\partial \rho_j}{\partial x_i} x_i \le 1 - \rho_{0j} + \sum_{i=1}^{N_{dv}} \frac{\partial \rho_j}{\partial x_i} x_{i0} \qquad (25)$$

In matrix form

$$A_2 x \le b_2 \qquad (26)$$

where $A_2 = \dfrac{\partial \rho}{\partial x}$ is of the dimension $N_e \times N_{dv}$.

x is a vector of design variables, i.e. the HRBFN parameters and has the dimension $N_{dv} \times 1$.

$$b_2 = \{1\}_{N_e \times 1} - \rho_{0j} + \sum_{i=1}^{N_{dv}} \frac{\partial \rho_j}{\partial x_i} x_{i0} \text{ is of the dimension } N_e \times 1$$

The constraint eq. (15) and (16) can together be put into matrix form by combining eq. (23) and (26) as

$$\begin{bmatrix} A_1 \\ A_2 \end{bmatrix} \{x\} \le \begin{Bmatrix} b_1 \\ b_2 \end{Bmatrix} \qquad (27)$$

Eq. (20) and (27) represent the standard form for LP problem. This SLP problem can be solved using commercial optimization toolbox available within MATLAB, MOSEK [reference] to name a few.

3.1.4 2-D Examples

This section presents examples to demonstrate the application of HRBFN to design 2-D and 3-D topologies. The examples demonstrate the use of coarse FEA mesh, mesh-independency, the application of perturbation and SLP algorithm and automated method to obtain optimal cutoff density.

    3.1.4.1 Demonstration of HRBFN based approach producing solution using coarse FEA meshs
    Figure 3.4 (a) shows a cantilever beam fixed at one end and horizontal axial loading at the other end. The objective is to get a minimum compliance design using 40% of the total material. The first example uses a coarse finite element analysis grid (8×4). Figure 3.4 (b) shows optimal topology obtained by traditional method (Sigmund *et al* [25]) using filtering scheme so that the top 40% densities are retained. Figure 3.4 (d) shows the optimal locations and shapes of HRBF network bases. Figure 3.4 (e) shows the topology obtained by HRBFN approach using 10 bases, same mesh size as that of SIMP method and the same filtering scheme. Figure 3.4 (c) shows unfiltered plot for the SIMP method with intermediate densities. Figure 3.4 (f) shows the result of perturbation algorithm (refer to section 3.1.3.1) which serves as a starting point for sequential linear programming. It is evident that the filtered plot for SIMP method does not provide a good idea about what the topology should look like. As opposed to that, the HRBFN approach provides a correct representation of topology and the topology is quite close to being "manufacturable". Note that the unfiltered plot for traditional topology shown in figure 3.4 (c) gives some idea about what the final topology should look like, but it is nowhere close to being "manufacturable" and consists of checkerboard patterns which are difficult to interpret. In more complicated structures, the unfiltered plots might be may lead to incorrect designs due to difficulty in interpreting checerboard patterns. The number of finite element analyses used for both the approaches were fixed to be 40. The value of compliance for HRBFN approach was 1.4941e-6 whereas the value of compliance for traditional approach was found to be 2.8384e-6. Note that the value of compliance in case of traditional SIMP

27

method might change significantly after manufacturing the desired structure since the topology needs to be modified for manufacturing. But in case of HRBFN approach the value of compliance would remain more or less the same since the topology obtained is already close to being manufacturable.

3.1.4.2 Demonstration of Mesh independency of HRBFN approach

The same problem in section 3.1.4.1 was solved using a finer mesh (20×10) and 15 basis functions. The topology resulting from HRBFN approach was similar to the one obtained using coarse mesh. Figure 3.5 shows topologies obtained from SIMP and HRBFN methods. It is evident that the classical SIMP method is mesh-dependent; whereas HRBFN approach does not depend on mesh size.
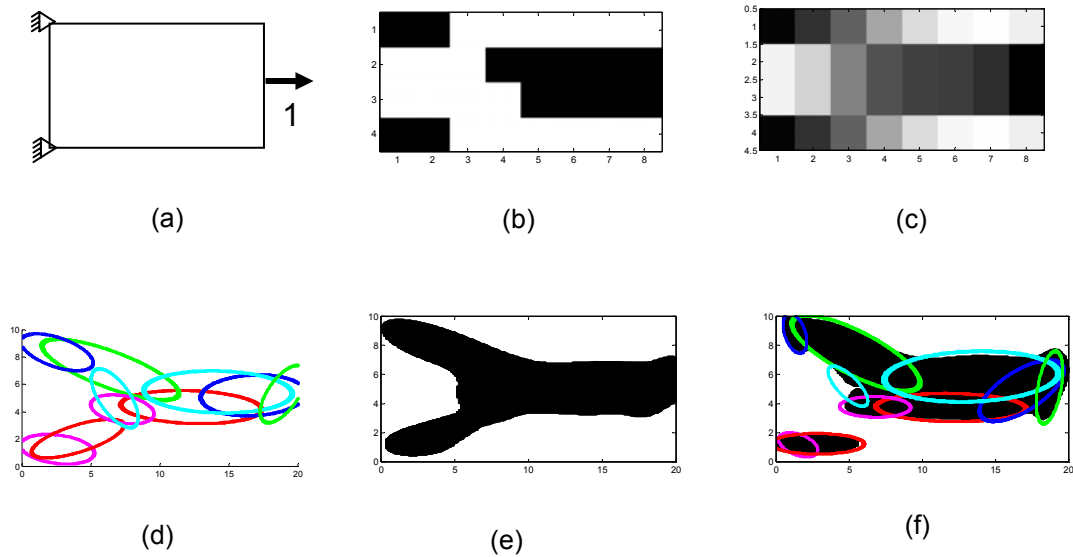
Figure 3.4 Demonstration of Mesh independency of HRBFN based approach: Coarse-mesh model. (a) Boundary conditions & loading (b) Result of SIMP based topology design by retaining the 40% of the densest elements. (c) Result of SIMP based topology design without filtering out intermediate densities. (d) Locations and shapes of hyper radial basis functions. (e) Result of perturbation algorithm for HRBFN based topology design by retaining 40% the densest network. (f) Result of Perturbation and SLP algorithm for HRBFN based topology design by retaining 40% the densest network.

Figure 3.5 Demonstration of Mesh independency of HRBFN based approach: Fine-mesh model. (a) Boundary conditions & loading (b) Result of SIMP based topology design without filtering out intermediate densities. (c) Locations and shapes of hyper radial basis functions. (d) Result of Perturbation and SLP algorithm for HRBFN based topology design by retaining 40% the densest network.

The selection of lower and upper bounds for HRBFN parameters is quite general and automated. The weight parameter can range from any negative to positive number to allow intricate concave shapes. The location parameter is such that the network base can be located anywhere within the rectangular area under consideration. The angle parameter is such that it allows for any orientation of network base. The width parameter is such that the network base can span entire rectangular area under consideration. The lower and upper bounds on HRBFN parameters for the example presented are as follows. For weight parameter $w_{Low} = 0,\ w_{High} = 1$ since we guess before hand that this topology would not require concave or other intricate shapes. For location parameter, $\overline{\mu}_{1Low} = 0,\ \overline{\mu}_{1High} = 20$, $\overline{\mu}_{2Low} = 0,\ \overline{\mu}_{2High} = 10$ since a rectangular plate of dimension 20 units in *x*-direction and 10

units in y-direction is considered. For width parameter, $\sigma_{1Low} = 0.5$, $\sigma_{1High} = 4$, $\sigma_{2Low} = 2$, $\sigma_{2High} = 40$ to ensure a network base is capable of spanning the entire breadth of the rectangular plate. For angle parameter, $\theta_{Low} = 0°$, $\theta_{High} = 180°$ to ensure a network base can be oriented in any direction. The lower and upper bounds for all the examples presented in this work were chosen similar to this example.

3.1.4.3 Demonstration HRBFN based approach for topology design of structure subject to multiple loads

This example presents application of HRBFN approach to design minimum compliance structure subject to multiple loading. The constraint is to use 40% of the total material. The topology was designed using 15 HRBF bases with finite element mesh size of 20×10. The number of bases to be selected is based on the anticipated topology. Note that each base (represented by 6 design variables) is capable of acting as a link in the final topology. Hence, the number of bases used in the design process must be greater than the maximum anticipated structural links in the final design. Although the 15 number of bases are not required, it demonstrates the robustness of the proposed scheme. Some of these 15 bases are not active (low values for weight variable) in the final design. Figure 3.6 shows topologies obtained from SIMP and HRBFN methods. It is of note that the proposed HRBFN approach and the traditional SIMP produce similar topologies. The topology resulting from HRBFN approach is more intuitive and close to being manufacturabe. Note that all examples presented in this work use fixed mesh size and fixed number of bases (i.e. they do not change during the design process). This is consistent with the fact that in practical applications, a designer does not have liberty to iteratively increase the number of finite elements and number of basis functions to guarantee convergence to exact topology. The size of finite element model is mostly governed by computing resources and time constraints.

30
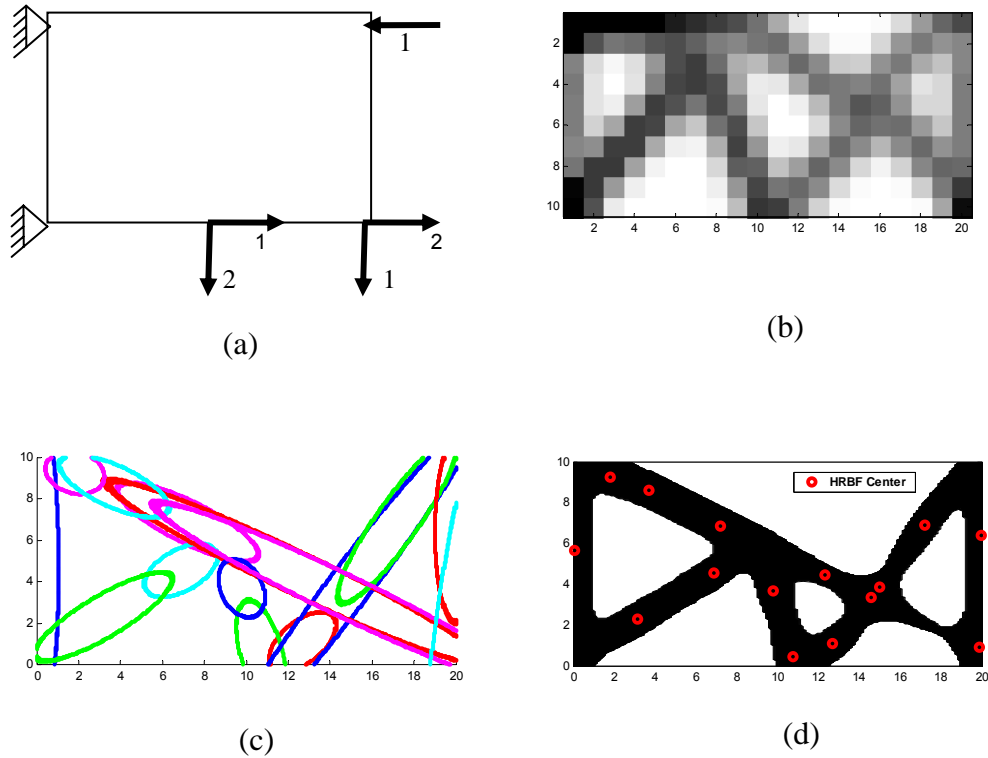
Figure 3.6 Demonstration of HRBFN based approach for multiple loads. (a) Boundary conditions & loading (b) Result of SIMP based topology design without filtering out intermediate densities. (c) Locations and shapes of hyper radial basis functions. (d) Result of Perturbation and SLP algorithm for HRBFN based topology design by retaining 40% the densest network.

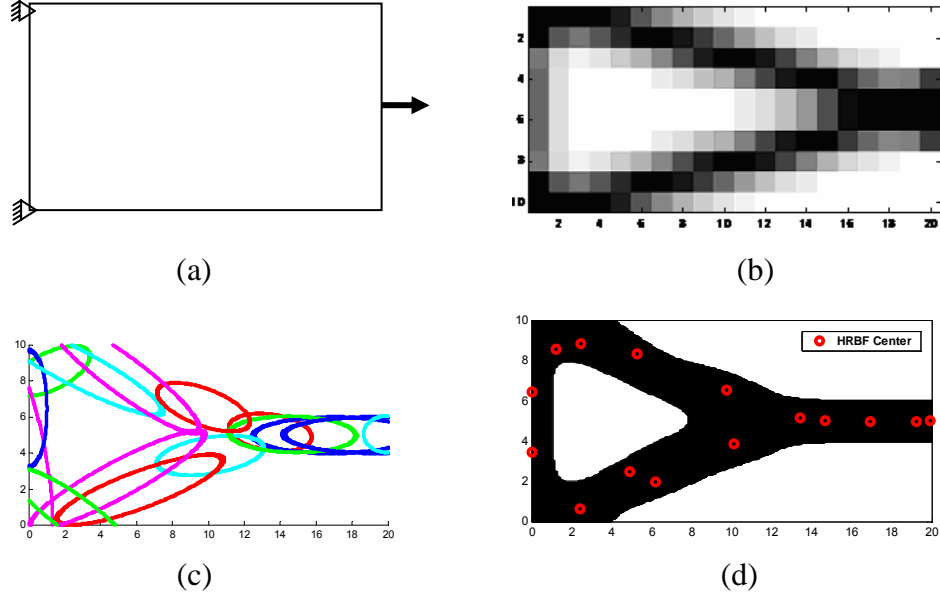3.1.4.4 Demonstration of HRBFN based approach for multi-objective topology design

This example presents application of HRBFN in design of minimum compliance structures with multiple objectives. Two objectives for this example are depicted in figure 3.7 (a) and (b). Note that the combined objective function used was an equally weighted sum of individual objectives. There are other objective formulations suggested in literature like K-S function (Kreisselmeier and Steinhauser, 1979) which would be worth investigating. But for the example presented, an equally-weighted sum worked well. The mesh size used was 20×20 elements. Figure 3.7 (c) shows optimal basis locations and shapes obtained by the proposed

31

approach with 10 bases. Figure 3.7 (d) shows the filtered topology obtained by the proposed approach.

(a)

(b)

(c)

(d)
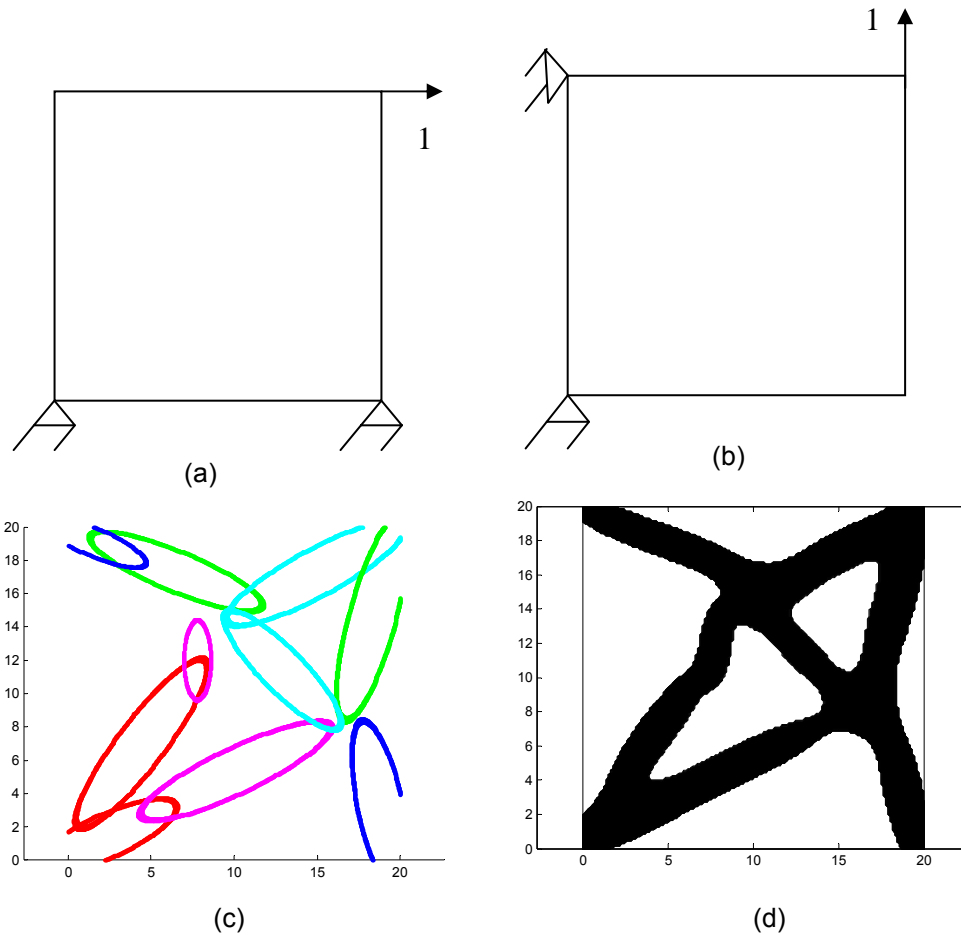
Figure 3.7 Demonstration of HRBFN based approach for multiple objectives. (a) Boundary conditions & loading for 1st objective (b) Boundary conditions & loading for 2nd objective. (c) Topology obtained by solving multi-objective problem with HRBFN approach. (d) Locations and shapes of optimal HRBF bases.

3.1.5 3-D Examples

The 3D examples presented demonstrate the application of HRBFN in 3D to design minimum compliance topologies. The three examples presented are minimum compliance topologies for stool, cantilever beam and coarse mesh with multiple loads.
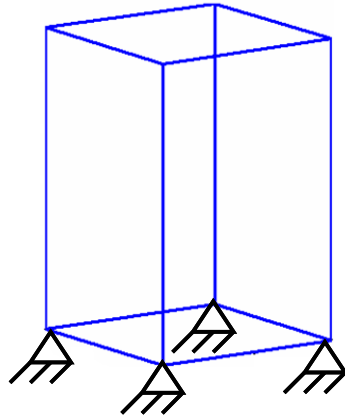
Figure 3.8 Problem Definition: Design of stool topology

Consider a cube with physical dimensions 40×40×60 units as shown in figure 3.8. A quarter-model was solved considering symmetry. The quarter model was meshed with 8-noded cubic elements with a grid-size 12×12×18. Four basis functions (40 design variables) were used to represent the structure. PSO was used to obtain starting point for sequential linear programming. Parallel processing was used to generate the swarm population for each iteration of PSO. The Cluster used for parallel processing consists of Dell PowerEdge 1950 dual quad core 2.33GHz Intel EM64T Xeon processors with 16GB of memory each. We had license to run 16 processes at a time. 25 hours were required to run 600 particle swarm iterations with population size of 128 per iteration. Starting from the PSO-solution, SLP was run for 200 iterations, which required 3 hours. Figure 3.9 shows the solution obtained from global optimizer PSO described in section 3.1.3.1. Figure 3.1.10 shows the final topology obtained by refining the global solution using SLP described in section 3.1.3.1. The total material usage was set to 40% (our trials indicate that the final topology is pretty much independent of this value). The final structure was obtained by retaining densities above the optimal density-level. The optimal density-level was computed based on graph shown in figure 3.11. Traditional SIMP design was obtained using the web-based tool developed by Tcherniak and Sigmund [26]. The topology

from traditional SIMP depends on the value of material fraction to be retained. Figure 3.12 shows traditional SIMP topologies for total volume fractions 40%, 30%, 20% and 5%. The proposed approach has clear advantage over traditional SIMP in terms of being independent of fraction total material usage constraint. The topology from proposed approach is free of jagged edged, checkerboards and close to being manufacturable.

Figure 3.9 Stool: Solution using Particle Swarm Optimization with parallel processing. Cluster consists of Dell PowerEdge 1950 dual quad core 2.33GHz Intel EM64T Xeon processors with 16GB of memory each. 25 hours were required to run 600 particle swarm iterations with population size of 128 per iteration (76800 objective evaluations).
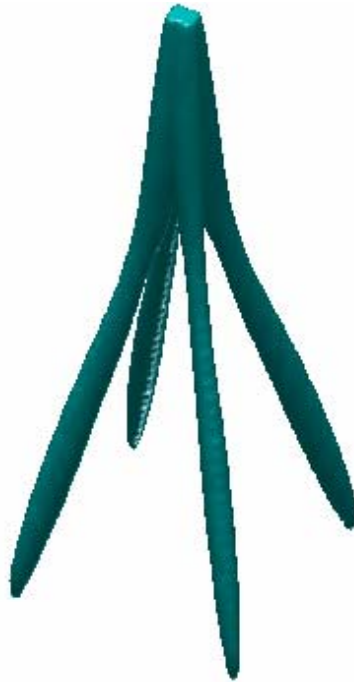
Figure 3.10 Stool: Solution using Sequential Linear Programming starting from the solution of Particle Swarm Optimization. 3 hours were required to run 200 sequential iterations.
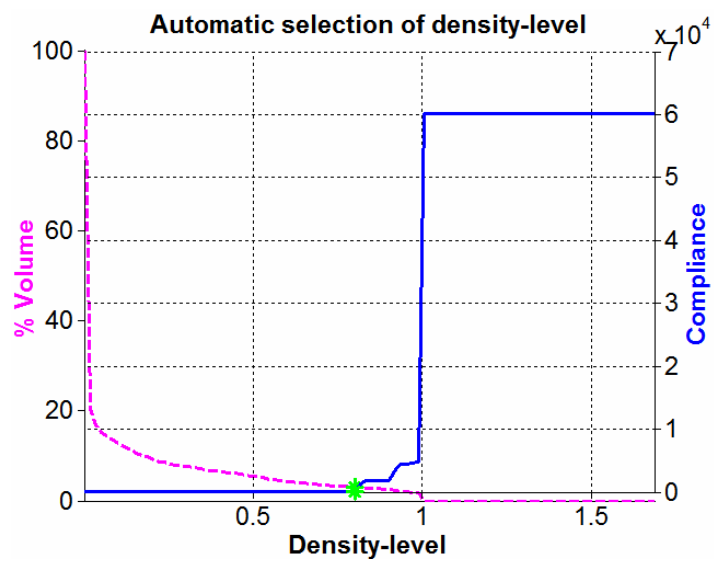
Figure 3.11 Stool: Automatic selection of optimal density level. The point marked by * is selected as the optimal density level since there is no further decrease in compliance with respect to density-level. The optimal density corresponds to 3% of the total volume

35
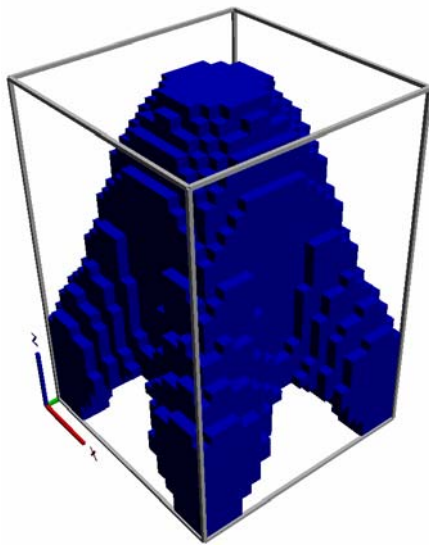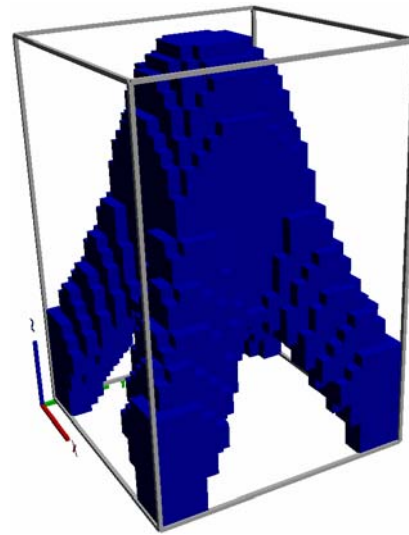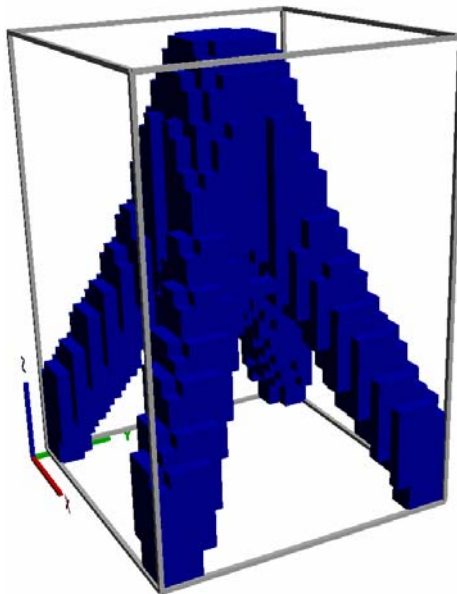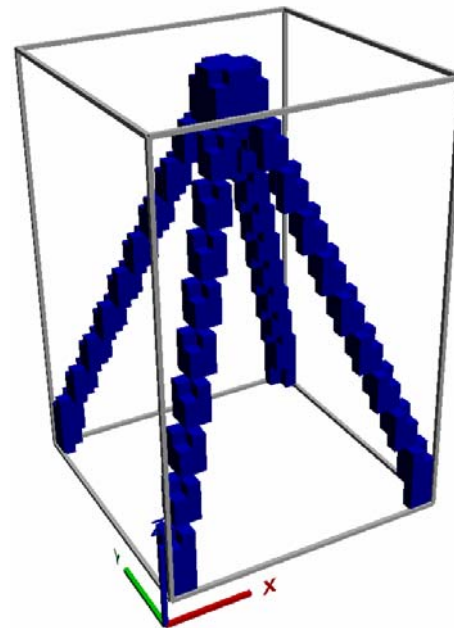
Figure 3.12 Stool: Traditional SIMP design for total volume fraction of
(a) 40% (b) 30% (c) 20% (d) 5%

3.1.5.2 Cantilever Beam

Consider a design domain with physical dimensions 10×3×16 units as shown in figure 3.13. The model was meshed with 8-noded cubic elements with a grid-size 10×4×16.
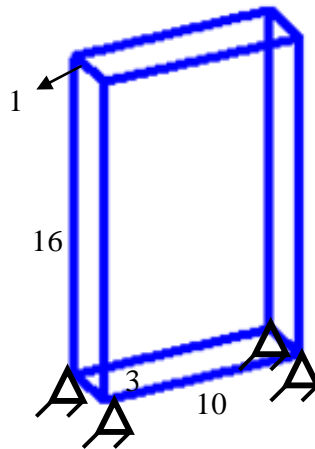
Figure 3.13 Design of Cantilever: Problem Definition

Twelve basis functions (120 design variables) were used to represent the structure. Total material fraction of 40% was used as a constraint. Perturbation and SLP algorithm was run on a PC with 2.13GHz processor and 2GB memory for 300 iterations each, which took about 3 hours. Figure 3.14 shows the topology obtained by HRBFN based approach. The optimal density-level was computed based on graph shown in figure 3.15. Figure 3.16 shows traditional SIMP topologies for total volume fractions 40%, 30% and 20%. The results produced by SIMP varied according to total volume fraction. As opposed to this, the HRBFN based approach provided an easy to interpret topology without a priori knowledge of the fraction material usage constraint.
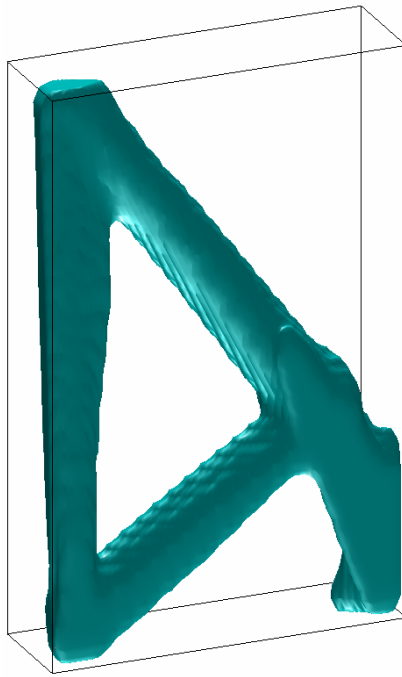
Figure 3.14 Cantilever: Solution using Perturbation and Sequential Linear Programming. 3 hours were required to run 600 sequential iterations.
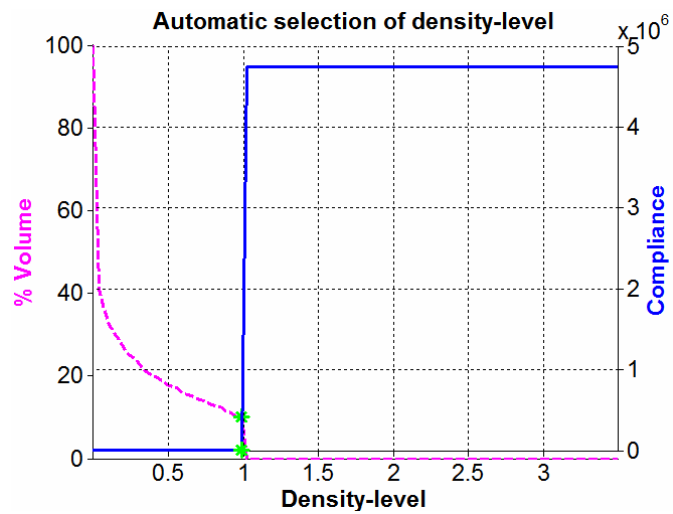
Figure 3.15 Cantilever: Automatic selection of optimal density level. The optimal density corresponds to 10% of the total volume

(a)   (b)   (c)
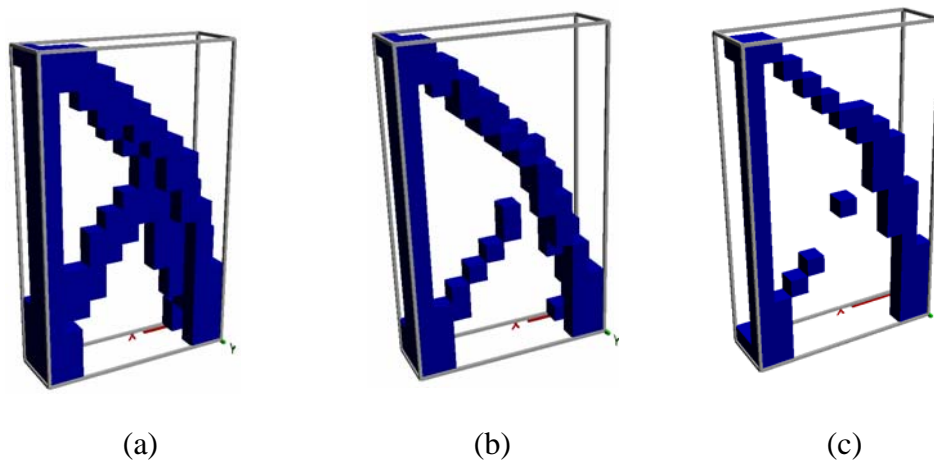
Figure 3.16 Cantilever: Traditional SIMP design for total volume fraction of
(a) 40% (b) 30% (c) 20%

3.1.5.3 Coarse mesh with multiple Loads

This example demonstrates the minimum compliance topology design for structure subject to multiple loads. The design domain is cube with physical dimensions 20×30×40 units. The domain is meshed with 8-noded cubic elements with a grid-size 6×6×11. Figure 3.17 shows loading and boundary conditions.
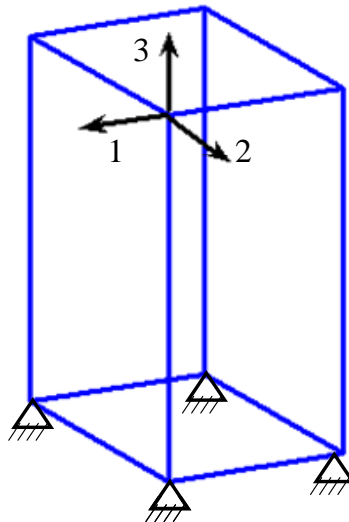
Figure 3.17 Coarse mesh with multiple Loads: Loading
and Boundary conditions.

Figures 3.18 and 3.19 show the designs obtained by proposed and traditional SIMP methods. Perturbation and SLP algorithm was run on a PC with 2.13GHz processor and 2GB memory. The computation-time for the proposed approach was approximately half an hour for 500 SLP iterations.

Figure 3.18 Coarse mesh with multiple Loads: Solution using Perturbation and Sequential Linear Programming. 30 minutes were required to run 600 sequential iterations.
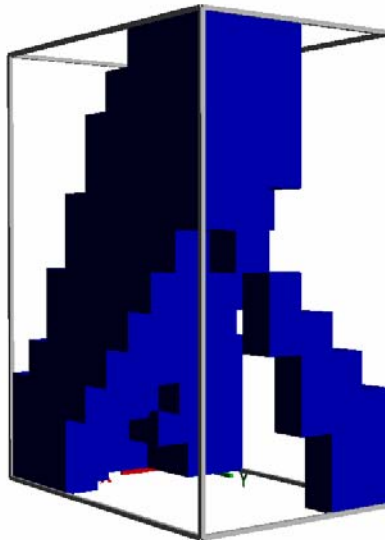
Figure 3.19 Coarse mesh with multiple Loads: Solution of traditional SIMP method

It is worth noting that, for all the examples, the proposed approach yields smooth, checkerboard-free topology which is easy to interpret and can be converted to parametric CAD solid model. On the other hand, the traditional SIMP design needs further interpretation and processing for conversion to CAD model. Koguchi and Kikuchi [27] recently proposed a surface reconstruction algorithm to convert the SIMP topology into parametric CAD model. Kumar and Gossard [28], Hsu [29] used the method of density contour to extract SIMP geometries. Our final structure is an iso-density surface at the optimal density level. The geometry-extraction step is unnecessary in our proposed approach. HRBFN, in principle can also be used to post-process SIMP results for conversion to CAD models. In this work a more comprehensive approach has been presented which is analogous to finding the optimal parameters of CAD model. The computation time can be further sped-up using an efficient compiled language like C or Java.
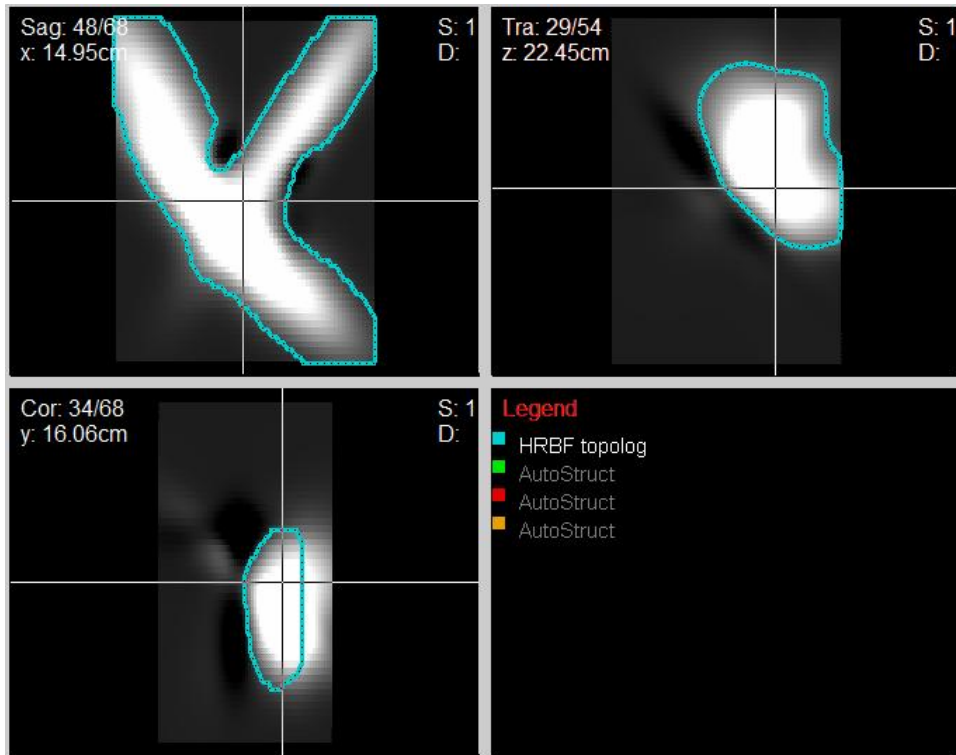
Figure 3.20 Use of CERR [26] in Topology Manipulation and Visualization

Open source software CERR (Computational Environment for Radiotherapy Research) [30], originally developed for radiotherapy research, was used to extract and visualize 3D topologies from the proposed HRBFN approach. CERR, along with our module for topology optimization, has methods for extracting geometry from 3D volumetric data, importing and exporting geometry in formats such as DICOM (Digital Image Communications in Medicine)[1], PLY (Polygon File Format)[2], and editing geometry. This software can be used to display topology optimization results from various algorithms or institutions simultaneously, determine consensus geometry (Myerson *et al* [31]) and image enhancement. Figure 3.20 is a snapshot of CERR showing three orthogonal views of the designed topology for the example presented in 3.1.5.3. The blue polygon shows the outline for structure at specific density level. It can be further edited interactively to satisfy manufacturing or any other criteria. The software developed provides a platform for sharing and evaluating results from various topology optimization methods.

<u>3.2 Maximum Fundamental Frequency Topology design</u>

In this section, the application of HRBFN to solve maximum fundamental natural frequency topology optimization problems is presented. The solution procedure is similar to that of the minimum compliance topology design. Problem formulation and sensitivity analysis are presented followed by 2-D examples.

3.2.1 Problem Statement

The optimization problem can be stated as follows

$$\text{Minimize } f = -\omega_1^{\,2} \tag{28}$$

Where ω_1 is the fundamental frequency of system (or structure) calculated by finite element analysis with the material density governed by HRBFN. For dynamic systems, the governing equation is

---

[1] http://medical.nema.org/ (Dec 01, 2009)
[2] http://en.wikipedia.org/wiki/PLY_(file_format) (Dec 01, 2009)

$$K\Phi = \omega^2 M\Phi \qquad (29)$$

where K is the global stiffness matrix assembled from the elemental stiffness matrices. M is the global mass matrix assembled from the elemental mass matrices using lumped mass formulation. ω represents natural frequency and $\Phi = \begin{bmatrix} \phi_1 & \phi_2 & ..... & \phi_n \end{bmatrix}$ represents modal matrix. The assembly of global stiffness and mass matrices is shown in equation 30.

$$K = \sum_{j=1}^{N_e} \left(\rho_j^{n^*} + \rho_{reg} \right)(K_e)_j , \quad M = \sum_{j=1}^{N_e} \left(\rho_j + \rho_{reg} \right)(M_e)_j \qquad (30)$$

where, $(K_e)_j$ and $(M_e)_j$ are the elemental stiffness and mass matrix for the jth element. The constraints for this problem are the total material usage, the bound for material density (greater than 0) and the bound constraints for HRBFN parameters as explained in section 3.1.1.

3.2.2 Sensitivity Analysis

The sensitivity of objective with respect to an HRBFN parameter is given by

$$\frac{d\left(-\omega_1^2\right)}{d\hbar_i} = -\frac{\phi_1^T \left(\dfrac{\partial K}{\partial \hbar_i} - \omega_1^2 \dfrac{\partial M}{\partial \hbar_i} \right)\phi_1}{\phi_1^T M \phi_1} \qquad (31)$$

where $\hbar_i$ is one of the six parameters for i^{th} basis function. $\dfrac{dK}{d\hbar_i}$ and $\dfrac{\partial M}{\partial \hbar_i}$ in eq. (31) can be computed analytically or by using approximate method like finite difference or complex variable method. In this work, the sensitivity was computed using analytical method and verified by the complex variable method. Differentiating eq. (30) w.r.t. parameter $\hbar_i$ we obtain

$$\frac{\partial K}{\partial \hbar} = \frac{\partial \sum_{j=1}^{N_e}\left(\rho_j^{n^*} + \rho_{reg} \right)(K_e)_j}{\partial \hbar_i} \text{ and } \frac{\partial M}{\partial \hbar} = \frac{\partial \sum_{j=1}^{N_e}\left(\rho_j + \rho_{reg} \right)(M_e)_j}{\partial \hbar_i} \qquad (32)$$

Substituting eq. (7) in eq. (32), we obtain

$$\frac{\partial K}{\partial \hbar} = \frac{\partial \sum_{j=1}^{N_e} \left(\sum_{i=1}^{r} w_i e^{-g_i^2} \right)^{n^*} (K_e)_j}{\partial \hbar_i} \quad \text{and} \quad \frac{\partial M}{\partial \hbar} = \frac{\partial \sum_{j=1}^{N_e} \left(\sum_{i=1}^{r} w_i e^{-g_i^2} \right)(M_e)_j}{\partial \hbar_i} \tag{33}$$

On further simplifying eq. (33), we obtain

$$\frac{\partial K}{\partial \hbar} = \sum_{j=1}^{N_e} \left(\sum_{i=1}^{r} \frac{\partial \left(w_i e^{-g_i^2} \right)^{n^*}}{\partial \hbar_i} \right)(K_e)_j \quad \text{and} \quad \frac{\partial M}{\partial \hbar} = \sum_{j=1}^{N_e} \left(\sum_{i=1}^{r} \frac{\partial \left(w_i e^{-g_i^2} \right)}{\partial \hbar_i} \right)(M_e)_j \tag{34}$$

Thus, the sensitivity of objective to HRBFN parameters can be obtained by substituting eq. (34) in eq. (31).

3.2.3 Examples

Two 2D examples are presented to demonstrate the maximum fundamental frequency topology design. The results are compared with traditional SIMP method. As a first example, consider a 12x6 units cantilever beam fixed at the bottom and loaded with mass at the top edge as shown in Figure 3.21 (a). The constraint is to use 40% of the total material. Figure 3.21 (b) shows optimal topology obtained by the SIMP method using 20×10 mesh. The problem was solved using the proposed HRBFN approach using 15 bases and the same mesh size. Figure 3.21 (c) shows optimal locations and shapes of the bases obtained by the proposed approach. Figure 3.1.21 (d) shows topology obtained by the proposed approach using filtering scheme so that the top 40% densities are retained. For the second example, consider a cantilever beam fixed at left end and mass attached to the other end as shown in Figure 3.22 (a). Figure 3.22 (b) shows optimal topology obtained by the density method using 20×10 mesh. In this case, the SIMP method did not converge for the 40% material usage constraint. Figure 3.22 (c) shows optimal basis locations and shapes obtained by the proposed approach with 15 bases and the same mesh size. Figure 3.1.22 (d) shows topology obtained by the proposed approach. These examples demonstrate that HRBFN based approach is able to produce easily interpretable topologies compared to the traditional SIMP method.
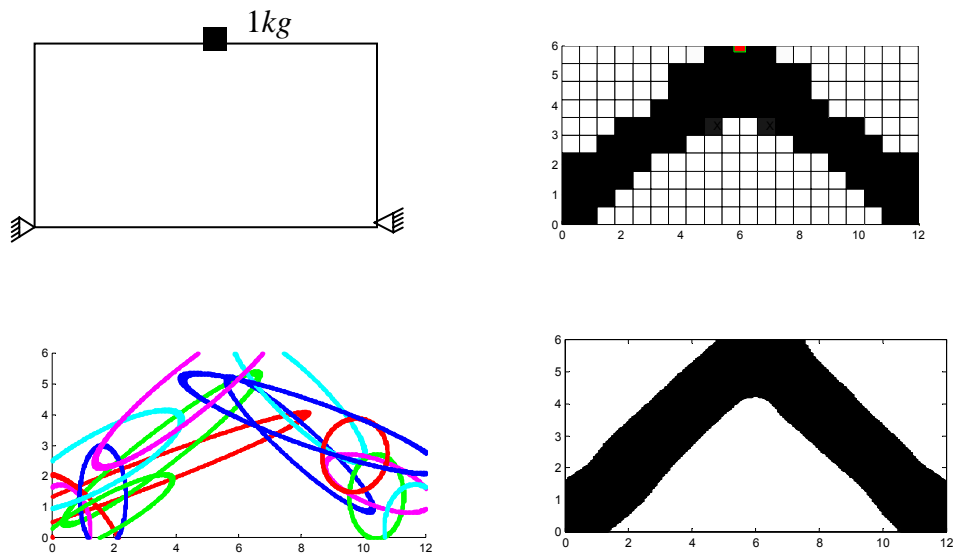
Figure 3.21 (a) Boundary conditions & loading (b) Result of SIMP Method (c) Locations and shapes of HRBF Bases (d) Result of HRBF based topology design

(a)

(b)

(c)

(d)
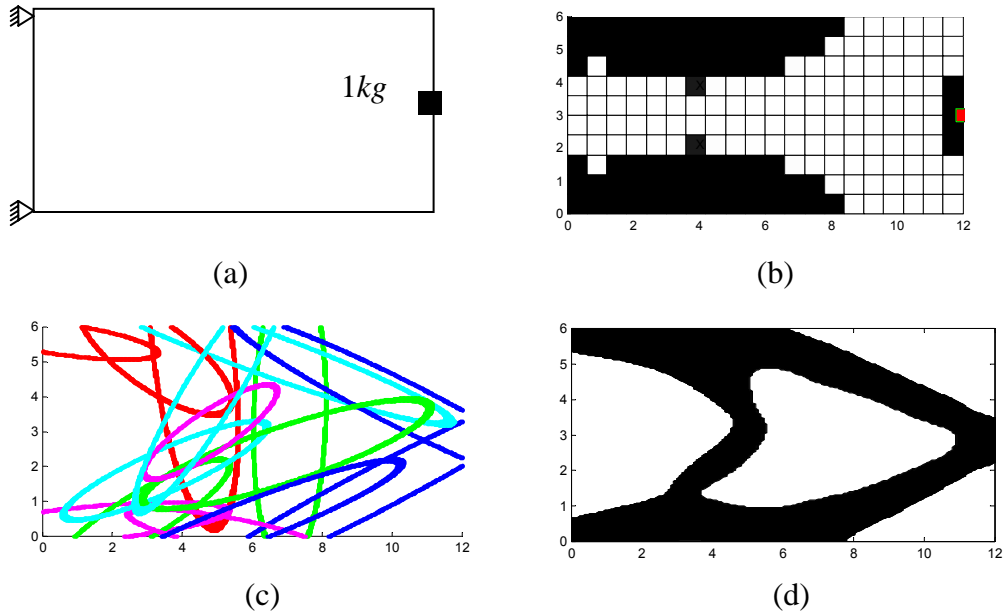
Figure 3.22 (a) Boundary conditions & loading (b) Result of SIMP Method. The solution did not converge for the selected constraint and selected solution parameters (c) Locations and shapes of HRBF Bases (d) Result of HRBF based topology design

3.3 Conclusion

This chapter presented the application of HRBFN to design 2D and 3D topologies for minimum compliance and maximum fundamental frequency objectives. Problem formulation was presented followed by analytical sensitivity analysis, solution procedure and examples. The optimization algorithm, which uses heuristic global optimizer followed by sequential linear programming, was presented. The HRBF results were compared with well established SIMP designs and found to be better interpretable and mesh-independent.

CHAPTER 4

DESIGN OF COMPLIANT MECHANISM

4.1 Introduction

A compliant mechanism transfers or transforms motion, force, or energy without using rigid links connected at movable joints [32]. Compliant mechanisms gain at least some of their mobility from the deflection of flexible members rather than from movable joints only. Some of the advantages of compliant mechanisms include the potential for a dramatic reduction in the total number of parts required to accomplish a specified task, ease of manufacturing, scalability (i.e. implemented in micro, meso and macro scales) and weight reduction. Hence they have a great deal of application in MEMS, robotics, medical devices and consumer products along with many other areas. But analyzing and designing such compliant mechanisms is a challenging task. Some of the difficulties in design include nonlinear relationship between geometry and elastic behavior and fatigue and hysteresis which can limit the performance. Moreover, the design problem has inherent multiple local minima. Hence, due to too many design variables involved, the traditional continuum based method SIMP is unable to provide a global solution. Since HRBFN representation of topology scales down the number of variables significantly, it is useful in this design. Multi-criteria optimization to minimize strain energy and maximize mutual energy simultaneously [33, 34, 35] is used in this work. The problem formulation proposed by [34] handles multiple input and output displacements. Since different sets of boundary conditions are applied to solve for mutual and strain energy, two sets of equations need to be solved. In this work we propose a reanalysis formulation [36, 37, 38, 39] to obtain the strain energy from the solution of mutual energy problem. This circumvents the need to solve two sets of equations separately and hence cuts-down the solution time by half.

The next sections describe problem formulation which includes sub-problems for mutual and strain energies along with the sensitivity analysis, reanalysis formulation to speed up analysis and the example of compliant motion inverter.

4.2 Problem formulation

A multi-criteria optimization approach is used to minimize strain energy and maximize mutual energy of the structure. The two sub-problems involved in this approach, namely, calculation of strain and mutual energy are described in this section. The design procedure and integration of HRBFN with FEA is explained with the help of an example compliant mechanism design problem for motion inverter depicted in figure 4.1.
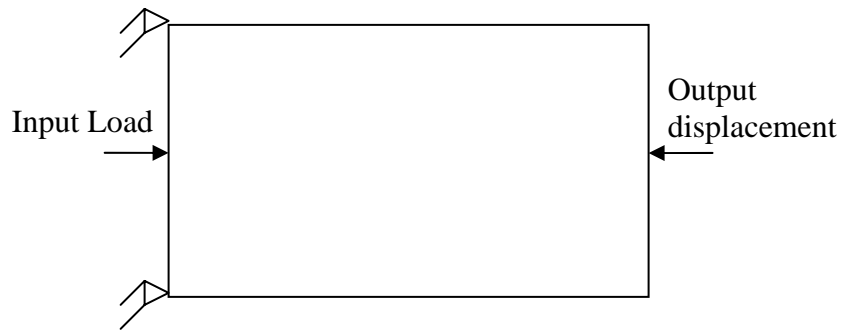
Figure 4.1 Compliant mechanism motion inverter

4.2.1 Mutual Energy (Kinematic function)

Kinematic function represents the flexibility of the structure for specified input loading and output displacements. It is stated as shown in eq. (35).

$$\text{Mutual Energy } = \ v_B{}^T K u_A \qquad\qquad (35)$$

K is the stiffness matrix of the structure and assembled as shown in eq. (36).

$$K = \sum_{j=1}^{N_e} \rho_j{}^{n^*} K_{ej} \qquad\qquad (36)$$

48

where $K_{e\,j}$ is the elemental stiffness matrix for the jth element, N_e is the number of elements for finite element analysis, ρ_j is the density of jth element and n^* is the power of density. $n^* = 4$ was used for the examples presented. The contribution of ith hyper radial basis function towards the density of jth finite element is shown in eq. (37).

$$\rho_j = \rho_j(Xe_j, Ye_j) = \sum_{i=1}^{r} w_i e^{-g_i^2} \tag{37}$$

where

$$g^2 = \Delta x^T \left[T^T\right] \begin{bmatrix} \dfrac{1}{\theta_{i1}} & 0 \\ 0 & \dfrac{1}{\theta_{i2}} \end{bmatrix} \left[T\right] \Delta x$$

$$T = \begin{bmatrix} \cos(\alpha_{i1}) & \sin(\alpha_{i1}) \\ -\sin(\alpha_{i1}) & \cos(\alpha_{i1}) \end{bmatrix},$$

$$\Delta x = \begin{Bmatrix} \overline{\mu}_1 - \mu_{i1} \\ \overline{\mu}_2 - \mu_{i2} \end{Bmatrix}, \quad X = \left(\overline{\mu}_1, \overline{\mu}_2\right) = \left(Xe_j, Ye_j\right)$$

w_i, $\left(\theta_{i1}, \theta_{i2}\right)$, $\left(\mu_{i1}, \mu_{i2}\right)$ and α_{i1} represent weight, width, location and orientation of ith basis respectively. The density across each element is assumed constant and evaluated at its centroidal coordinates $\left(Xe_j, Ye_j\right)$. u_A and v_B in eq. (35) are displacement vectors obtained by solving the system of equations represented by figures 4.2 (a) and (b) respectively.

(a)   (b)
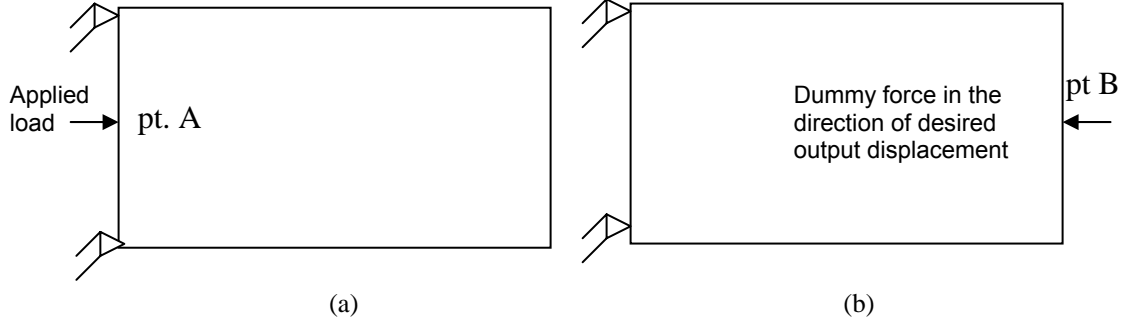
Figure 4.2 (a) Calculation of displacement vector u_A by solving $K u_A = f_A$ (b) Calculation of displacement vector v_B by solving $K v_B = f_B$

4.2.2 Strain Energy (Structural function)

Structural function represents the stiffness of the structure. It is stated as shown in eq. (38).

$$\text{Strain Energy} = u_{se}{}^T K u_{se} \qquad (38)$$

where K is the global stiffness matrix of the structure assembled from eqs. (36) and (37), u_{se} is the displacement vector obtained by solving the system of equations represented by figure 4.3. Note that the system represented in figure 4 has less degrees of freedom as compared to the one used for calculating the mutual energy.
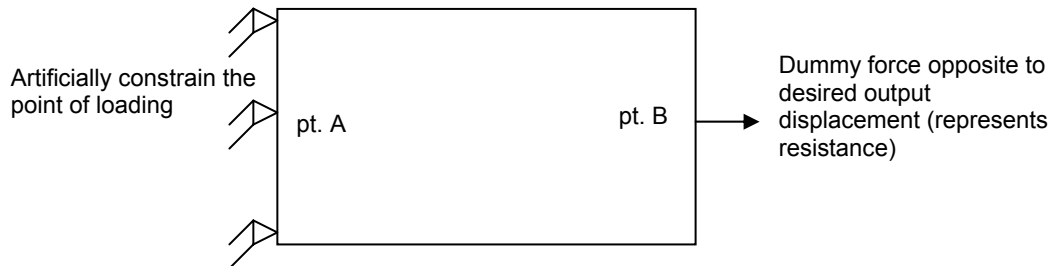
Figure 4.3 Calculation of displacement vector u_{se} by solving $K u_{se} = f_{se}$

50

4.3 Optimization Problem Formulation and Solution Procedure

The optimization problem has multiple criteria to minimize the strain energy and maximize the mutual energy simultaneously. The design variables are the parameters governing the HRBFN. The problem is stated in eq. (39)

Calculate the density of each finite element to minimize

$$f = -\frac{\text{Mutual Energy}}{\text{Strain Energy}} = -\frac{v_B{}^T K u_A}{u_{se}{}^T K u_{se}} \tag{39}$$

subject to the total material usage and bound constraints.

The optimization problem stated in eq. (39) is solved using the two-step (global + local search) algorithm mentioned in Chapter 4. The analytical sensitivity analysis required to obtain fast convergence is described in next section.

4.4 Sensitivity Analysis

For the multi-criteria objective represented by eq. (40), the sensitivity is given by

$$f' = \frac{(\text{Strain Energy})'*(\text{Mutual Energy}) - (\text{Strain Energy})*(\text{Mutual Energy})'}{(\text{Strain Energy})^2} \tag{40}$$

where $(\ )'$ represents derivative with respect to one of the design variables (i.e. one of the HRBFN parameters). Now let's calculate the sensitivity of strain energy and mutual energy separately. Differentiating eq. (38), we get

$$(\text{Strain Energy})' = 2u_{se}(x)^T K u_{se}(x)' + u_{se}(x)^T K(x)' u_{se}(x) \tag{41}$$

The notation $u_{se}(x)$ is used to represents the fact that u_{se} is a function of x. For equilibrium of system shown in figure 4.3,

$$K u_{se} = f_{se} \tag{42}$$

Differentiating both sides of eq. (42) and pre-multiplying by $u_{se}(x)^T$, we get

$$u_{se}(x)^T K(x)' u_{se}(x) = -u_{se}(x)^T K(x) u_{se}(x)' \tag{43}$$

Substituting eq. (43) into eq. (41), we get

$$(\text{Strain Energy})' = -u_{se}(x)^T K(x)' u_{se}(x) \tag{44}$$

Eq. (44) can be used to calculate the sensitivity of strain energy w.r.t. the design variable. Now, in order to compute sensitivity of mutual energy, let's differentiate eq. (35) w.r.t. a design variable

$$(\text{Mutual Energy})' = \left(v_B(x)^T\right)' K(x) u_A(x) + v_B(x)^T K(x)' u_A(x) + v_B(x)^T K(x) u_A(x)' \tag{45}$$

For equilibrium of system shown in figure 4.2 (a),

$$K u_A = f_A \tag{46}$$

Differentiating both sides of eq. (46) and pre-multiplying by $v_B(x)^T$, we get

$$v_B(x)^T K(x)' u_A(x) = -v_B(x)^T K(x) u_A(x)' \tag{47}$$

For equilibrium of system shown in figure 4.2 (b),

$$K v_B = f_B \tag{48}$$

Differentiating both sides of eq. (48) and post-multiplying by $u_A(x)$, we get

$$\left(v_B(x)^T\right)' K(x) u_A(x) = -v_B(x)^T K(x)' u_A(x) \tag{49}$$

Substituting eq. (48) and (49) in (45), we get

$$(\text{Mutual Energy})' = -v_B(x)^T K(x)' u_A(x) \tag{50}$$

$K(x)'$ in eqs. 44 and 50 can be computed analytically from eq. 36. Differentiating eq. 36 w.r.t. one of the parameters for i^{th} basis, we obtain

$$K(x)' = \frac{\partial \sum_{j=1}^{N_e} \left(\rho_j^{n^*} + \rho_{reg}\right)(K_e)_j}{\partial x} \tag{51}$$

where x can be one of the basis parameters $w_i, \theta_{i1}, \theta_{i2}, \mu_{i1}, \mu_{i2}, \alpha_{i1}$

Substituting eq. 37 in eq. 51, $K(x)'$ can be further simplified as

$$K(x)' = \sum_{j=1}^{N_e} \left(\frac{\partial \left(w_i e^{-g_i^2} \right)^{n^*}}{\partial x} \right) (K_e)_j \tag{52}$$

Thus, the sensitivity of multi-criteria objective function can be computed by substituting eqs. (35), (38), (44) and (50) in eq. (40).

4.5 Reanalysis Formulation

Reanalysis techniques (Arora 1976, Krisch 1993, Krisch and Liu 1997, Chen et al 1999) [36, 37, 38, 39] are used to reduce the computation cost for repetitive simulations after modifying initial structure. As described in section 4.2, the design procedure requires solution of two sets of equations, one for mutual energy and the other for strain energy due to different boundary conditions. The inversion of stiffness matrix for solving the above equations is computationally expensive. In this section we propose a reanalysis formulation for introducing additional constraints to a system to avoid inverting the stiffness matrix twice.
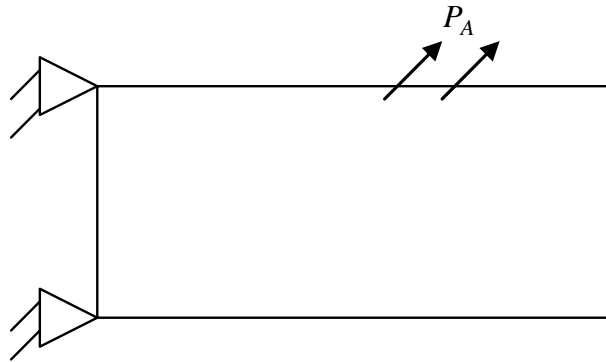
Figure 4.4: Model A (more degrees of freedom than model B)

Let figure 4.4 represent a structural system corresponding to the one used in calculating mutual energy. This system will be referred to as model A. K_A, P_A and u_A be the stiffness matrix, load vector and displacement vectors for model A respectively, taking into consideration the applied boundary conditions. Then, we have,

$$K_A u_A = P_A \qquad (53)$$

Now, let us introduce additional constraints (boundary conditions) to model A. Let's also change the loading as represented in figure 4.5. This system, which corresponds to the one used in calculating strain energy, will be referred to as model B. Then, model B is governed by the following system of equations.

$$K_B u_B = P_B \qquad (54)$$

where K_B, P_B, u_B are the stiffness matrix, load vector and displacement vectors for model B respectively, taking into consideration the applied boundary conditions.
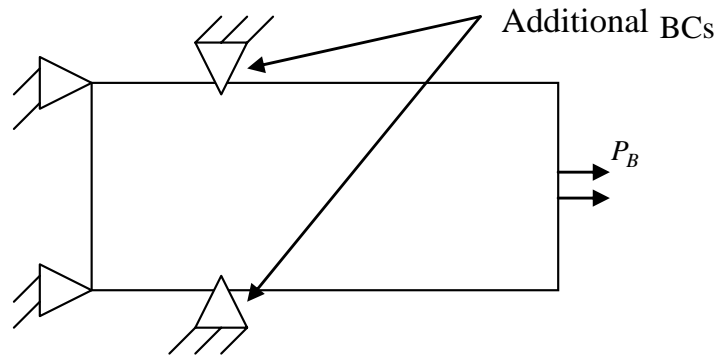
Figure 4.5: Model B (less degrees of freedom than model A)

Since model A has more degrees of freedom than model B, let's partition the matrix and vectors as follows.

$$K_A = \begin{bmatrix} K_B & K_{AR} \\ K_{RA} & K_{RR} \end{bmatrix} \qquad (55)$$

$$u_A = \begin{Bmatrix} u_B \\ u_R \end{Bmatrix} \tag{56}$$

$$P_A = \begin{Bmatrix} P_B \\ R \end{Bmatrix} \tag{57}$$

where u_B, u_R and R are unknown vectors. Define,

$$P_A = \begin{Bmatrix} P_B \\ 0 \end{Bmatrix} + \begin{Bmatrix} 0 \\ R \end{Bmatrix} \tag{58}$$

or

$$P_A = \widehat{P}_B + [W]R \tag{59}$$

Where $\widehat{P}_B = \begin{Bmatrix} P_B \\ 0 \end{Bmatrix} \tag{60}$

$$[W] = \begin{Bmatrix} 0 \\ I \end{Bmatrix} \tag{61}$$

Substituting eq. (59) in eq. (53), we get

$$K_A u_A = \widehat{P}_B + [W]R \tag{62}$$

Thus,

$$u_A = K_A^{-1} \widehat{P}_B + K_A^{-1} WR \tag{63}$$

Define,

$$u_{B_A} = K_A^{-1} \widehat{P}_B \tag{64}$$

$$Y_W = K_A^{-1} W \tag{65}$$

Then eq. (63) becomes

$$u_A = u_{B_A} + Y_W R \tag{66}$$

Referring to eq. (56), eq. (66) can be written in partitioned form as

$$\left\{ \begin{array}{c} u_B \\ u_R = 0 \end{array} \right\} = \left\{ \begin{array}{c} \left(u_{B_A}\right)_B \\ \left(u_{B_A}\right)_R \end{array} \right\} + \left[\begin{array}{c} Y_{W_B} \\ Y_{W_R} \end{array} \right] R \tag{67}$$

From the lower portion of eq. (67), we get

$$0 = \left(u_{B_A}\right)_R + Y_{W_R} R \tag{68}$$

From eq. (68), R can be calculated as

$$R = \left(Y_{W_R}\right)^{-1} \left(u_{B_A}\right)_R \tag{69}$$

Once $\{R\}$ is known, we can compute u_B from the top portion of eq. (33) as follows

$$u_B = \left(u_{B_A}\right)_B + Y_{W_B} R \tag{70}$$

Eq. (70) is the reanalysis solution of u_B. Note that in this formulation, the required data,

u_{B_A} and Y_W are computed from model A (eqs. 64 and 65). Thus we do not need to solve eq. 54

directly. The reanalysis formulation derived above can be used to compute u_{se} in eq. 42 from

the solution of mutual energy sub-problem.

4.6 Example

The design procedure described above was applied to design motion inverter shown in

figure 4.1. Symmetry was used to design only the top half of domain. The symmetry boundary

conditions are shown in fig. 4.6. The physical dimensions of the domain before symmetry were
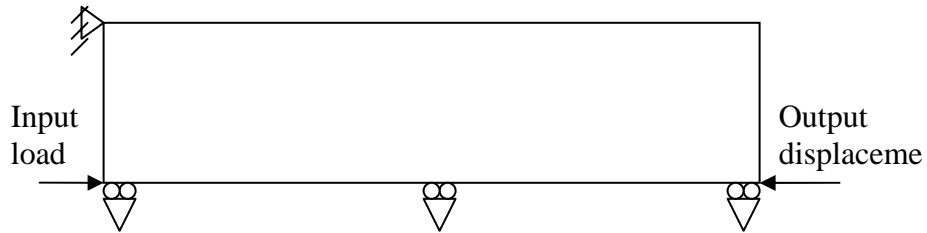
Figure 4.6: Symmetry boundary conditions for design of motion inverter

20×10 units. The mesh-size used for finite element analysis after imposing symmetry was 20×10. The constraint for total material to be retained was set at 10%. Note that unlike traditional SIMP, there was no upper limit of 1 for elemental pseudo-density as explained in section 3.1.1. 12 basis functions were used to design the compliant mechanism. 12800 function evaluations (16 parallel processors) were used to obtain an approximate global solution with PSO. 400 SLP iterations were used to further refine the approximate global solution. Figure 4.7 shows the optimal locations, shapes and orientations of hyper radial basis functions obtained after SLP. Figure 4.8 shows the final topology of compliant motion inverter obtained using the proposed approach. The boundary of structure is the iso-density contour of HRBFN.
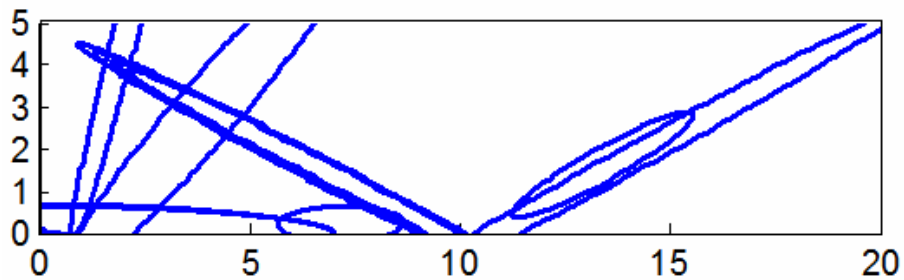
Figure 4.7 Location, shape and orientation of hyper radial bases for symmetric model
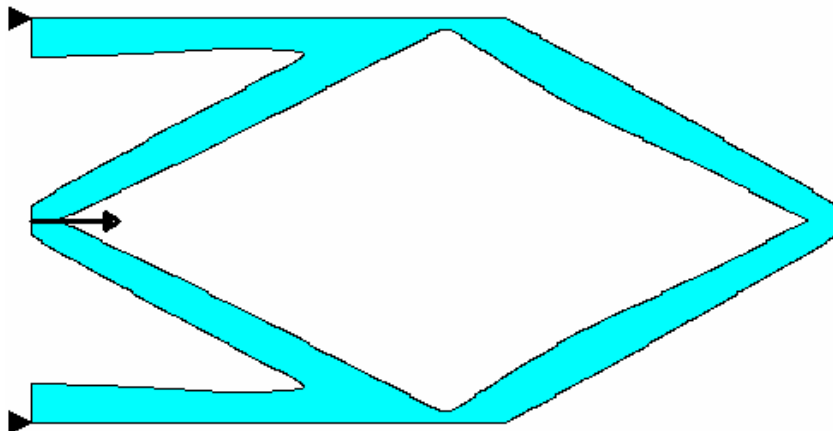
Figure 4.8 Topology design for Motion Inverter using HRBFN

The value of optimal density level can be obtained from visual inspection or using an automated level selection suggested in section 3.1.5.1. This makes a priori knowledge of fraction volume or the use of adaptive fraction volume selection algorithms not necessary for the proposed approach.

4.7 Conclusion

A global solution for designing compliant mechanism using continuum based topology optimization method was presented. The proposed HRBFN approach parameterizes structural geometry with small number of parameters, which makes the global solution possible. Exact reanalysis formulation was used which cuts down the finite element analysis time by half. An example design for motion inverter was presented. The design produced was free of checkerboards, smooth and close to being manufacturable. Moreover the design process is fully automated, where a priori knowledge of fraction material to be retained is not necessary.

CHAPTER 5

IMAGE RECONSTRUCTION FOR OPTICAL MEDICAL IMAGING

5.1 Introduction

This chapter presents the application of HRBFN based topology design in optical image reconstruction. Diffusion optical tomography [40] is a technique of using near infrared (NIR) light in the wavelength range of 700 to 1000 nm to probe light scattering media, such as thick biological tissues, in order to derive images of their scattering and absorption coefficients $(\mu_s{}', \mu_a)$. The goal of optical tomography is to reconstruct distribution of the optical coefficients within a spatial domain Ω based on the measurement made on the boundary $\partial\Omega$. Mathematically, the reconstruction of optical coefficients in optical tomography is a nonlinear, multi-minima inverse problem. The equation that models light propagation in highly scattering media, such as breast and brain tissues, is the diffusion equation. This equation is derived from the Boltzmann equation [41] with the assumptions (i) anisotropic radiance (ii) change of flux much lower than collision frequency. The simplified diffusion equation is then stated as

$$\nabla(k\nabla u(r)) - \mu_a u(r) = 0 \text{ where } r \in \Omega; \ u = u_s \text{ at the optical source and } k = \frac{1}{3(\mu_a + \mu_s{}')}.$$

The two main challenges in optical tomography are to: (i) solve the diffusion equation so as to obtain the fluence distribution of light at various points along the boundary of the tissue, given the distribution of optical properties within the medium (known as the forward problem), and (ii) estimate the optical properties of the medium by matching the forward model to the experimentally obtained boundary measurements (known as the inverse problem). Typically, finite element or difference methods are used to solve the diffusion equation. In order to estimate the optical properties, an approach similar to topology optimization is used. Hence, the

59

design variables are the optical properties of each finite element. Using a description function to represent optical properties would lead to reduction in number of design variables and also help get rid or artifacts due to checkerboards in topology optimization. In this work, hyper radial basis function is used to represent the distribution of optical properties and the diffusion equation is solved using finite element method.

5.1.1 Critical wavelength-range and its application

Biological materials are relatively transparent to light in the NIR range and hence permit photon transmission in a relatively large depth. Absorption and scattering are two phenomena that affect the propagation of light in biological tissues, and scattering is the dominant phenomenon for light in the NIR range as shown in figure 5.1.
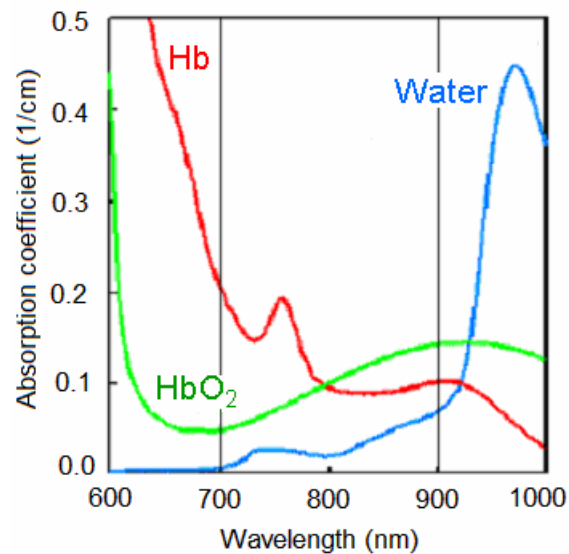
Figure 5.1 Wavelength v/s μ_a (Liu *et al* [42])

The absorption and scattering coefficients, known as the optical properties, describe the likelihood that a photon, which is injected into the biological material, is absorbed or scattered over some given distance. Absorption occurs at specific wavelengths, that is, absorption is wavelength dependent and is determined by the molecular properties of the tissue

60

or biological material. Scattering is caused by a refractive index mismatch at the boundaries of cell membranes and intracellular organelles. With knowledge of the optical properties, it is possible to determine the vascular saturation of hemoglobin [42] (or the oxygen saturation of blood), the blood volume and various metabolic activities of biological materials. These parameters may be clinically important in predicting the response of tumor to radiation therapy, chemotherapy and/or overall tumor prognosis. Determination of the optical properties is done by image reconstruction.

5.1.2 Literature review

Three kinds of image reconstruction techniques [43] are found in the literature, namely, the time resolved method, the frequency domain method, and the continuous intensity method (DC). In a time resolved case, an ultra-short pulsed laser is used as the light source and the temporal distribution of the light emerging from the tissue surface is detected using either a synchronous scan streak camera with picoseconds' time resolution or a time-correlated single photon counting (TCSPC) system. In the frequency domain method, a radio frequency modulated light source is used to illuminate an object and the phase and modulation depth of the transmitted light are measured, usually using a heterodyne detection method. Both the time resolved and frequency domain schemes exhibit high temporal resolutions (in the picoseconds range for the time resolved and nanosecond for the frequency domain). However, tomographic measurements made with the time resolved technology require data-acquisition time on a time frame of minutes to derive data having acceptable low noise levels. In addition, they have the disadvantages of high cost and complexity in the equipment. In the DC case, a point laser source with constant intensity is used to continuously illuminate the object and the amplitude of the outgoing light on the boundary is measured. Though continuous intensity system has the advantage of low cost and relatively high signal to noise ratio (SNR), it presents difficulty in simultaneous unique recovery of diffusion and absorption coefficients and inability to probe objects embedded deep inside the medium.

The equation that models light propagation in highly scattering media, such as breast and brain tissues, is the diffusion equation. This equation is derived from the Boltzmann equation with the assumptions of (i) anisotropic radiance (ii) change of flux much lower than collision frequency. The equation is further simplified assuming a time step of unity. The simplified diffusion equation is then stated as $\nabla(k\nabla u(r)) - \mu_a u(r) = 0$ where $r \in \Omega$; $u = u_s$ at the optical source and $k = \dfrac{1}{3(\mu_a + \mu_s')}$. The two main challenges in optical tomography are: (i) to solve the diffusion equation so as to obtain the optical flounce distribution of light at various points along the boundary of the tissue, given the distribution of optical properties within the medium (known as the forward problem), and (ii) to estimate the optical properties of the medium by matching the forward model to the experimentally obtained boundary measurements (known as the inverse problem).

Majority of reconstruction schemes use the finite element or finite difference method to solve the forward problem and an optimization or perturbation algorithm to solve the inverse problem. Different types of boundary conditions [44] applicable to the problem can be found in the literature. These boundary conditions include (a) Dirichlet condition at boundary (b) Dirichlet condition at extrapolated boundary, matched refractive index (c) Robin condition, matched refractive index (d) Dirichlet condition at extrapolated boundary, mismatched refractive index (e) Robin condition and mismatched refractive index. The exact boundary condition to be used is not yet fully understood and should be verified experimentally. In this work the Dirichlet condition at boundary is used. Simon Arridge [40, 41, 42, 43, 44, 45, 46] is one of the pioneers in this field and has developed Time-Resolved Optical Scattering and Absorption Tomography software for image reconstruction at University College, London. It is based on solving forward and inverse problems as stated earlier. Klibonov *et al* [47] have developed an Elliptic Systems Method that derives and linearizes the inverse problem to a well-posed boundary value problem for a coupled system of elliptic partial differential equations. Brian Pogue *et al* [49, 50] have

reconstructed images solving the inverse problem using the Levenberg-Marquardt optimization scheme. Yong Xu *et al* [51] have used regularized Newton approach to optimize the inverse problem objective function. Andreas Hielscher [52] used the perturbation method to solve the inverse problem. It is worth noting that most of the previous work heeds more attention towards locating the abnormality than estimating exact absorption and scattering coefficients.

Apart from noninvasive determination of the oxygenation level within biological tissues, there has been research in the use of this technique for obtaining tomographic images of the neonatal head, with a view of determining oxygenation and deoxygenation levels of blood. The diffusion approximation of the Boltzmann transport equation is not valid in the regions of low scatter such as the cerebrospinal fluid found in neonatal heads. Methods have been proposed for dealing with non-scattering regions within diffusing materials, like the one proposed by Arridge *et al* through the use of radiosity-diffusion model. Huabei Jiang [53] presented a third order approximation to diffusion equation for imaging brain tissues. Taufiquar Khan and Huabei Jiang [54] suggested diffusion approximation to radiative transport equation for scattering media with spatially varying refractive indices. In this work photon transport is modeled using second order diffusion equation.

5.2 Forward Problem in Optical Tomography

The forward model in optical tomography can be briefly described as shown in figure 5.2. In the forward model the distribution of optical properties (μ_s' and μ_a) in a tissue sample under study are known. Also the light intensity at source position (u_s) is given. The
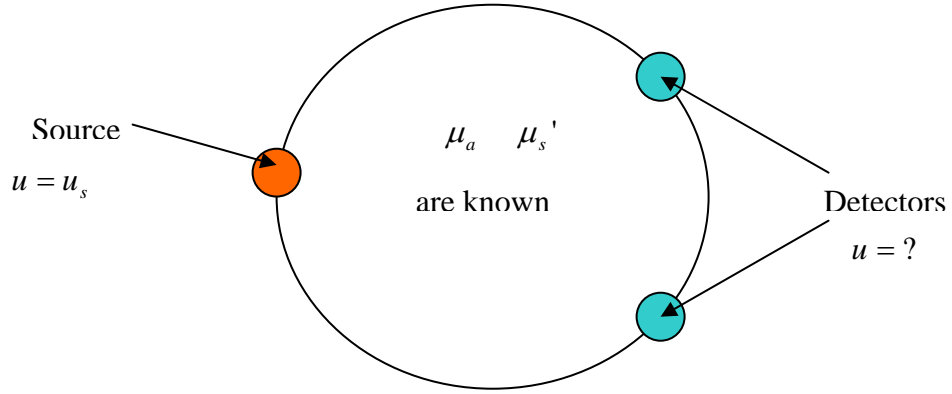
Figure 5.2 The Forward Problem in Optical Tomography

optical fluence rates at the detector locations will be determined by solving the forward model as follows. The light fluence rate in tissues depends upon absorption and scattering coefficients. The equation used to model light propagation within tissues is the diffusion approximation to the radiative transport equation or Boltzmann equation. Thus, the governing equation for this time-invariant case is

$$\nabla(k\nabla u(r)) - \mu_a u(r) = 0 \qquad (71)$$

where $r = \Omega$ and $u = u_s$ at the optical source $\qquad\qquad$ (72)

Also, $k = \dfrac{1}{3(\mu_a + \mu_s')}$ $\qquad\qquad$ (73)

A finite element approximation to equation (20) and (21) can be expressed as

$$(K_k(k) + K_a(\mu_\alpha))u = 0 \qquad (74)$$

Subject to the boundary condition

$$u_j = u_s \qquad (75)$$

where u_s is the source strength and j is a node on the boundary $\partial\Omega$ where the source is located. Note that K_k and K_a are assembled from the element matrices according to standard finite element procedures. Please refer to the appendix D for the finite element formulation.

$$K_k = \sum (K_e)_k \tag{76}$$

$$K_a = \sum (K_e)_{\mu_a} \tag{77}$$

Before applying the boundary conditions, we have

$$KU = 0 \tag{78}$$

Since we know the source strength, assuming a point source, we can partition U as

$$U = \begin{Bmatrix} U_s \\ U_f \end{Bmatrix} \tag{79}$$

Partitioning K accordingly leads equation (74) to

$$\begin{bmatrix} K_{ss} & K_{sf} \\ K_{fs} & K_{ff} \end{bmatrix} \begin{Bmatrix} U_s \\ U_f \end{Bmatrix} = \begin{Bmatrix} 0 \\ 0 \end{Bmatrix} \tag{80}$$

Then U_f can be computed from

$$K_{ff} U_f = -K_{fs} U_s \tag{81}$$

The global stiffness matrix K can be assembled from the following equation

$$K = \sum k (K_e)_k + \sum \mu_a (K_e)_{\mu_a} \tag{82}$$

where $(K_e)_k = \int_{A_e} [\phi']^T [\phi'] dxdy \tag{83}$

$$(K_e)_{\mu_a} = \int_{A_e} [\phi]^T [\phi] dxdy \tag{84}$$

Where $[\phi]$ = shape function matrix. Please refer the appendices A to C for derivation of shape functions.

Within each element, k and μ_a are function of the hyper radial basis parameters.

$$\mu_a(x_c, y_c) = C_{a0} + \sum_{i=1}^{N} C_{ai} e^{-\left[\frac{(x_c - \overline{x_{ai}})^2}{\sigma_{axi}} + \frac{(y_c - \overline{y_{ai}})^2}{\sigma_{ayi}} \right]} \tag{85}$$

where (x_c, y_c) are the coordinates of centroid of the element, N is the number of tumors, C_{a0}, C_{ai}, σ_{axi}, σ_{ayi}, $\overline{x_{ai}}$ and $\overline{y_{ai}}$ are the hyper radial basis parameters.

$$\mu_s'(x_c, y_c) = C_{s0} + \sum_{i=1}^{N} C_{si} e^{-\left[\frac{(x_c - \overline{x_{si}})^2}{\sigma_{sxi}} + \frac{(y_c - \overline{y_{si}})^2}{\sigma_{syi}} \right]} \tag{86}$$

where (x_c, y_c) are the coordinates of centroid of an element, N is the number of hyper radial basis functions, C_{s0}, C_{si}, σ_{sxi}, σ_{syi}, $\overline{x_{si}}$ and $\overline{y_{si}}$ are the hyper radial basis parameters.

5.3 Inverse Problem in Optical Tomography

The inverse problem is one where the distribution of optical properties (μ_s' and μ_a) is unknown. We know the fluence intensity at source (u_s) and detectors. In order to obtain the distribution of optical properties, we use a numerical optimization technique. We start from an initial guess and minimize the least square error function using an optimization subroutine. A brief algorithm used to solve this inverse problem is stated as follows.

Let $U_{ij}^{(m)}$ = Measured u at node i when the light source is at j.

U_{ij} = Corresponding computed value.

The inverse problem can be stated as follows.

Given the fluence measurements $U_{ij}^{(m)}$,

Calculate μ_a, $\mu_s' = \mu_a\left(C_{a0}, C_{ai}, \sigma_{axi}, \sigma_{ayi}, x_{ai}, y_{ai}\right)$, $\mu_s'\left(C_{s0}, C_{si}, \sigma_{sxi}, \sigma_{syi}, x_{si}, y_{si}\right)$

To minimize $f = \sum_{j=1}^{Ns} \sum_{i=1}^{Np} (U_{ij} - U_{ij}^{(m)})^2$ (87)

Following is a brief description of solution algorithm used.

1. Start from initial guess

$$(\mu_a, \mu_s') = \mu_a(C_{a0}, C_{ai}, \sigma_{axi}, \sigma_{ayi}, x_{ai}, y_{ai}), \mu_s'(C_{s0}, C_{si}, \sigma_{sxi}, \sigma_{syi}, x_{si}, y_{si}).$$

2. Use equation (82) to compute stiffness K. For each light Source,

   (a) Compute fluence intensity u using equation (28)

   (b) Compute contribution to error $e^T e$

   where $e = b^T u - \overline{u}^m$ (88)

   $\overline{u}^m$ = all measured data for this light source.

   b^T = Boolean matrix (composed of 0 and 1's so that $b^T u = u$ at measured

   point)

3. Update $\mu_a, \mu_s' = \mu_a(C_{a0}, C_{ai}, \sigma_{axi}, \sigma_{ayi}, x_{ai}, y_{ai}), \mu_s'(C_{s0}, C_{si}, \sigma_{sxi}, \sigma_{syi}, x_{si}, y_{si})$ using

   quadratic approximation with trust region approach implemented via MATLAB

   optimization toolbox.

Using equation (88), equation (87) can be written as

$$f = \sum_{j=1}^{Ns} (e_j^T e_j)$$ (89)

where $e_j = b^T \{u\}_j - \overline{u}_j^{(m)}$

where N_s is the number of sources, N_p is the number of detectors and b^T = Boolean matrix

(composed of 0 and 1's so that $b^T u = u$ at measured point).

In order to help convergence, sensitivity analysis is the crux of inverse problem. In this work analytical sensitivity analysis is derived as follows. If we want to use gradients in the optimizer, we need to calculate $\dfrac{\partial f}{\partial \alpha_i}$ (α_i is a design parameter). From equation (89), we have

$$\frac{\partial f}{\partial \alpha_i} = 2\sum e_j^T \frac{\partial e_j}{\partial \alpha_i}, \qquad (90)$$

Then using equation (88), we obtain

$$\frac{\partial e_j}{\partial \alpha_i} = b^T \frac{\partial \{u\}_j}{\partial \alpha_i} \qquad (91)$$

Substitution of equation (91) in equation (90) leads to

$$\frac{\partial f}{\partial \alpha_i} = 2\sum e_j^T b^T \frac{\partial \{u\}_j}{\partial \alpha_i} \qquad (92)$$

Thus, $\dfrac{\partial f}{\partial \alpha_i}$ depends on $\dfrac{\partial \{u\}_j}{\partial \alpha}$, which can be computed by sensitivity analysis as follows.

Differentiating eq. 81 with respect to design parameter α gives

$$\frac{\partial K_{ff}}{\partial \alpha_i} U_f + K_{ff} \frac{\partial U_f}{\partial \alpha_i} = -\frac{\partial K_{fs}}{\partial \alpha_i} U_s - K_{fs} \frac{\partial U_s}{\partial \alpha_i} \qquad (93)$$

where i represents the ith design parameter.

Since U_s is constant (known intensity of light source) $\dfrac{\partial U_s}{\partial \alpha_i} = 0$.

Then equation (93) leads to

$$\frac{\partial U_f}{\partial \alpha_i} = -K_{ff}^{-1} \left(\frac{\partial K_{fs}}{\partial \alpha_i} U_s + \frac{\partial K_{ff}}{\partial \alpha_i} U_f \right) \qquad (94)$$

Recall $\quad U = \begin{Bmatrix} U_s \\ U_f \end{Bmatrix}$

Then, $\quad \dfrac{\partial U}{\partial \alpha_i} = \begin{Bmatrix} \dfrac{\partial U_s}{\partial \alpha_i} \\ \dfrac{\partial U_f}{\partial \alpha_i} \end{Bmatrix} = \begin{Bmatrix} 0 \\ \dfrac{\partial U_f}{\partial \alpha_i} \end{Bmatrix} = \dfrac{\partial \{U\}}{\partial \alpha_i}$ \hfill (95)

Thus, the gradient is computed substituting equation (95) and (91) in equation (90).

Now, if we want to use Hessian in the optimizer, we need to have $\dfrac{\partial^2 f}{\partial \alpha_k \partial \alpha_i}$ (α_i and α_k are

design parameters). From equation (90)

$$\frac{\partial^2 f}{\partial \alpha_k \partial \alpha_i} = 2\sum \left(\frac{\partial e_j^T}{\partial \alpha_k} \frac{\partial e_j}{\partial \alpha_i} + e_j^T \frac{\partial^2 e_j}{\partial \alpha_k \partial \alpha_i} \right)$$ \hfill (96)

Using equation (88)

$$\frac{\partial^2 e_j}{\partial \alpha_k \partial \alpha_i} = b^T \frac{\partial^2 \{u\}_j}{\partial \alpha_k \partial \alpha_i}$$ \hfill (97)

Substituting equations (90) and (97) in equation (96)

$$\frac{\partial^2 f}{\partial \alpha_k \partial \alpha_i} = 2\sum \left(b \frac{\partial \{u\}^T}{\partial \alpha_k} b^T \frac{\partial \{u\}}{\partial \alpha_i} + \left(b^T \{u\}_j - \overline{u}^{(m)} \right)^T b^T \frac{\partial^2 \{u\}}{\partial \alpha_k \partial \alpha_i} \right)$$ \hfill (98)

Thus, $\dfrac{\partial^2 f}{\partial \alpha_k \partial \alpha_i}$ depends on $\dfrac{\partial^2 \{u\}}{\partial \alpha_k \partial \alpha_i}$ and $\dfrac{\partial \{u\}}{\partial \alpha_i}$.

$\dfrac{\partial \{u\}}{\partial \alpha_i}$ is already calculated in equation (95) and $\dfrac{\partial^2 \{u\}}{\partial \alpha_k \partial \alpha_i}$ can be computed by sensitivity

analysis of 1st order sensitivity as follows.

From equation (93), since $\dfrac{\partial U_s}{\partial \alpha_i} = 0$

$$\frac{\partial K_{ff}}{\partial \alpha_i} U_f + K_{ff} \frac{\partial U_f}{\partial \alpha_i} = -\frac{\partial K_{fs}}{\partial \alpha_i} U_s \tag{99}$$

Differentiating equation (99) with respect to α_k

$$\frac{\partial^2 K_{ff}}{\partial \alpha_k \partial \alpha_i} U_f + \frac{\partial K_{ff}}{\partial \alpha_i} \frac{\partial U_f}{\partial \alpha_k} + \frac{\partial K_{ff}}{\partial \alpha_k} \frac{\partial U_f}{\partial \alpha_i} + K_{ff} \frac{\partial^2 U_f}{\partial \alpha_k \partial \alpha_i} = -\frac{\partial^2 K_{fs}}{\partial \alpha_k \partial \alpha_i} U_s \tag{100}$$

Then equation (100) leads to

$$\frac{\partial^2 U_f}{\partial \alpha_k \partial \alpha_i} = -Kff^{-1} \left(\frac{\partial^2 K_{fs}}{\partial \alpha_k \partial \alpha_i} U_s + \frac{\partial^2 K_{ff}}{\partial \alpha_k \partial \alpha_i} U_f + \frac{\partial K_{ff}}{\partial \alpha_i} \frac{\partial U_f}{\partial \alpha_k} + \frac{\partial K_{ff}}{\partial \alpha_k} \frac{\partial U_f}{\partial \alpha_i} \right) \tag{101}$$

$$\text{Then,} \quad \frac{\partial^2 U}{\partial \alpha_k \partial \alpha_i} = \left\{ \begin{array}{c} \dfrac{\partial^2 U_s}{\partial \alpha_k \partial \alpha_i} \\[2mm] \dfrac{\partial^2 U_f}{\partial \alpha_k \partial \alpha_i} \end{array} \right\} = \left\{ \begin{array}{c} 0 \\[2mm] \dfrac{\partial^2 U_f}{\partial \alpha_k \partial \alpha_i} \end{array} \right\} = \frac{\partial^2 \{U\}}{\partial \alpha_k \partial \alpha_i} \tag{102}$$

Thus, the Hessian is computed substituting equation (102) and (97) in equation (96).

5.5 Example

An example presented in this section illustrates the application of HRBFN in detecting abnormalities (tumors) within normal tissues. Figure 5.3 represents simulated phantom model.
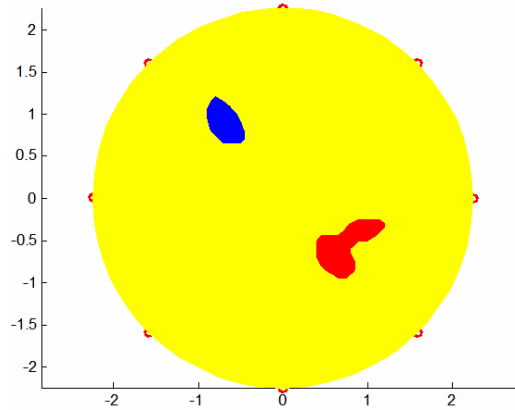
Figure 5.3 Simulated tissue and tumor model for Optical Tomography

The region in yellow represents normal tissue whereas regions in blue and red represent tumors with absorption coefficients 0.13 and 0.2 cm $^{-1}$. The forward problem is solved and the detector intensities are obtained at locations shown by red circular markers. Figure 5.4 shows finite element mesh along with detector locations used to solve the inverse problem. A 3-noded triangular element is used in FEA.
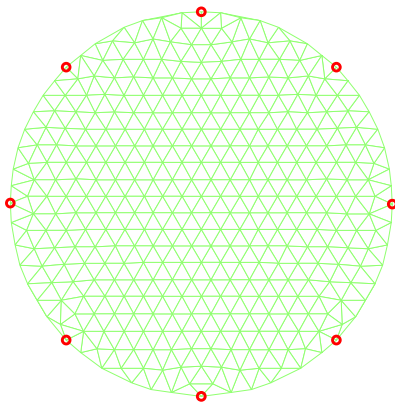
Figure 5.4 FEA mesh and location of source/detector pairs
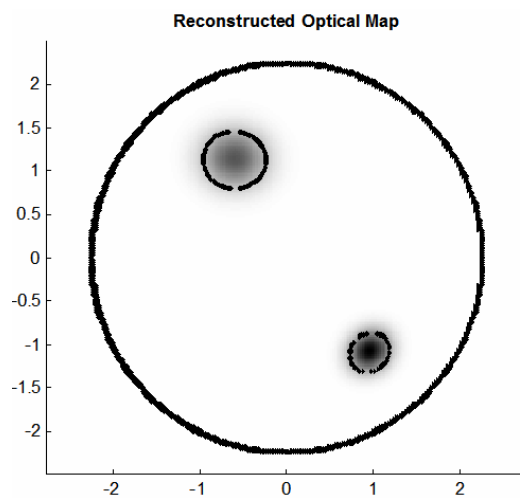
Figure 5.5 Reconstructed Optical map

Figure 5.5 shows the result of solving inverse problem using three bases in HRBFN. The design variables in the optimization problem were the HRBFN parameters representing absorption and scattering coefficients of tumor/s. It can be observed that the optical map of tumors represented in Figure 5.3 is not exactly reconstructed (figure 5.5). This can be attributed to the fact that the optical image reconstruction problem is ill-posed with multiple minima. A global optimization method to reach the exact solution needs further investigation.

<div align="center">5.6 Conclusion</div>

The application of HRBFN for optical image reconstruction was presented in this chapter. Finite element formulation was presented to solve the forward problem. The optimization procedure to reconstruct optical map from the detector measurements was presented. An example showing reconstruction of optical map for a simulated phantom was presented. The result was encouraging; but needs further improvements to reconstruct the optical map in terms of location as well as absorption and scattering coefficients.

CHAPTER 6

CONCLUSION AND FUTURE WORK

6.1 Conclusion

This dissertation presented the application of HRBFN as a topology description function for topology optimization. Application of HRBFN to various types of topology optimization problems, namely, compliance minimization, fundamental frequency maximization, compliant mechanism, optical tomographic imaging, was demonstrated. A robust optimization algorithm was developed using heuristic global optimizer and sequential linear programming. Objective function was evaluated in parallel to generate swarm population for the global optimizer. The proposed parallel processing would be useful to take advantage of ever increasing computing power; with multi-core processors and clusters becoming routine. The traditional SIMP method requires a priori knowledge about the fraction of material to be retained. This makes SIMP method prone to human interpretation and leads to errors. A simple modification to the traditional formulation, which makes SIMP method independent of a priori knowledge of fraction material to be retained and gets rid of checkerboards was proposed. The topologies obtained for the example problems attempted were free of checkerboard patterns, easily interpretable and close to being "manufacturable", thus demonstrating the potential of the proposed approach. With the use of HRBFN, the actual values of objectives (frequency, output displacement etc.) of manufactured topology would be quite close to those obtained from theoretical topology design. This would be useful in designing topologies for sophisticated applications (e.g. compliant mechanisms) where the objective function values (e.g. output displacement of compliant mechanism) are critical.

Some of the original contributions arising from this work include

(1)   Development of orient-able hyper radial basis function network and its application to topology optimization problems.

(2)   Development of global optimization algorithm for solution of topology optimization problems with multiple minima.

(3)   Algorithm for automatic selection of optimal fraction volume to be retained.

(4)   Development of reanalysis formulation for design of compliant mechanisms which results in cut-down of analysis-time by half.

(5)   Application of topology optimization technique for image reconstruction in optical tomography.

The concepts and tools developed are available in the form open-source, Matlab software which can be further modified for research use.

6.2 Future Work

The future work includes

(1) The use of HRBFN to post process SIMP results. Please refer to appendix E for an example of post processing tool for 2D topologies.

(2) Automated methods to select density level in order to obtain structures with optimal or redundant load paths with some factor of safety.

(3) Integration of approximate reanalysis techniques to avoid inversion of huge stiffness matrix for small system changes.

(4) The application of basis functions other than the Gaussian for HRBFN.

The next section provides an example of post processing tool for 2D topologies.

APPENDIX A

SHAPE FUNCTIONS FOR 4-NODED QUADRILATERAL ELEMENT

A four-nodded rectangular element is used in finite element analysis of rectangular geometry. The shape functions for this element are derived as follows.

Let $u = fa = \sum_{i=1}^{4} u_i N_i$

Where $f = [1 \ x \ xy \ y]$ and $a = [a1 \ a2 \ a3 \ a4]^T$

The element under consideration has a width W and height H. The nodal coordinates of this element are $XY = \begin{bmatrix} 0 & 0 \\ W & 0 \\ W & H \\ 0 & H \end{bmatrix}$

Then compute the matrix $A = f \ at \ XY$. This gives $A = \begin{bmatrix} 1 & 0 & 0 & 0 \\ 1 & W & 0 & 0 \\ 1 & W & H & WH \\ 1 & 0 & H & 0 \end{bmatrix}$

The shape function matrix $N = fA^{-1} = \begin{bmatrix} 1 - x/W - y/H + x*y/W/H \\ x/W - x*y/W/H \\ x*y/W/H \\ y/H - x*y/W/H \end{bmatrix}$

APPENDIX B

SHAPE FUNCTIONS FOR 3-NODED TRIANGULAR ELEMENT

A three-nodded triangular element is used in finite element analysis of 2D geometry with arbitrary shape. The shape functions for this element are derived as follows.

Let $u = fa = \sum_{i=1}^{4} u_i N_i$

Where $f = [1 \; x \; y]$ and $a = [a1 \; a2 \; a3]^T$

The element under consideration has coordinates (x1, y1), (x2, y2) and (x3, y3). The nodal

coordinates of this element are $XY = \begin{bmatrix} x1 & y1 \\ x2 & y2 \\ x3 & y3 \end{bmatrix}$

Then compute the matrix $A = f \; at \; XY$. This gives $A = \begin{bmatrix} 1 & x1 & y2 \\ 1 & x2 & y2 \\ 1 & x3 & y3 \end{bmatrix}$ `

The shape function matrix

$$N = fA^{-1} = \begin{bmatrix} [-(x2*y3-y*x2-x*y3+y*x3-y2*x3+x*y2)/(x2-x1)/(-y3+y2)] \\ [\;(x1*y3-y2*x3-x*y3+x*y2+y*x3-y*x1)/(x2-x1)/(-y3+y2)] \\ [\qquad\qquad\qquad -(-y2+y)/(-y3+y2)] \end{bmatrix}$$

APPENDIX C

SHAPE FUNCTIONS FOR 8-NODED CUBOID ELEMENT

An eight-nodded rectangular element is used in finite element analysis of cuboid geometry. The shape functions for this element are derived as follows.

Let $u = fa = \sum_{i=1}^{4} u_i N_i$

Where $f = [1 \quad x \quad y \quad z \quad xy \quad yz \quad zx \quad xyz]$ and $a = [a1 \quad a2 \quad a3 \quad a4 \quad a5 \quad a6 \quad a7 \quad a8]^T$

The element under consideration has a width W and height H. The nodal coordinates of this element are

$$XY = \begin{bmatrix} 0 & 0 & 0 \\ 0 & W & 0 \\ -L & W & 0 \\ -L & 0 & 0 \\ 0 & 0 & -H \\ 0 & W & -H \\ -L & W & -H \\ -L & 0 & -H \end{bmatrix}$$

Then compute the matrix $A = f$ at XY. This gives

$$A = \begin{bmatrix} 1 & 0 & 0 & 0 & 0 & 0 & 0 & 0 \\ 1 & 0 & W & 0 & 0 & 0 & 0 & 0 \\ 1 & -L & W & 0 & -LW & 0 & 0 & 0 \\ 1 & -L & 0 & 0 & 0 & 0 & 0 & 0 \\ 1 & 0 & 0 & -H & 0 & 0 & 0 & 0 \\ 1 & 0 & W & -H & 0 & -WH & 0 & 0 \\ 1 & -L & W & -H & -LW & -WH & HL & LWH \\ 1 & -L & 0 & -H & 0 & 0 & HL & 0 \end{bmatrix}$$

The shape function matrix

$N = fA^{-1}$
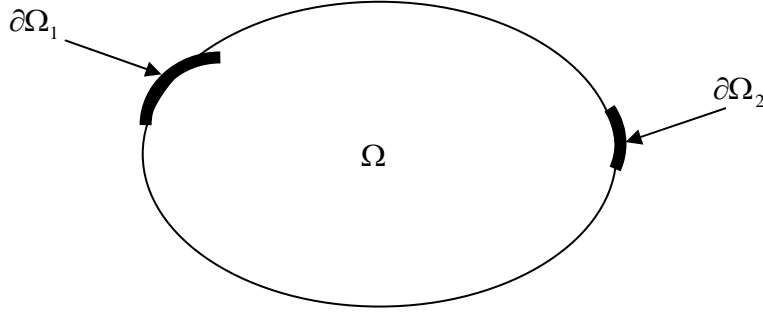
$$N = \begin{bmatrix} - (-W*H*L - x*W*H + y*H*L - z*W*L + x*y*H + y*z*L - z*x*W + x*y*z)/W/H/L \\ y*(H*L + x*H + z*L + z*x)/W/H/L \\ - x*y*(H+z)/W/H/L \\ x*(-W*H + y*H - z*W + y*z)/W/H/L \\ z*(-W*L + y*L - x*W + x*y)/W/H/L \\ - y*z*(L+x)/W/H/L \\ x*y*z/W/H/L \\ - z*x*(-W+y)/W/H/L \end{bmatrix}$$

APPENDIX D

FINITE ELEMENT FORMULATION FOR OPTICAL TOMOGRAPHY

Given the boundary value problem

$$-\nabla(k\nabla u) + \mu_a u - f = 0 \tag{d.1}$$

The Finite Element of above boundary value problem is derived using the weak formulation.

Following are the steps used for weak formulation:

1. Multiply the PDE with a *test function* and integrate the result over the domain.

2. Insert the boundary condition.

Let *v* be the test function. Then proceeding by the above steps,

$$\int_\Omega v(-\nabla(k\nabla u) + \mu_a u - f)dxdy = 0 \tag{d.2}$$

Note that

$$\nabla \bullet (vk\nabla u) = k\nabla u\nabla v + v\nabla \bullet (ku)$$

$$v\nabla \bullet (ku) = \nabla \bullet (vk\nabla u) - k\nabla u\nabla v \tag{d.3}$$

Substituting (d.3) into (d.2),

$$\int_\Omega (k\nabla u\nabla v + \mu_a uv - fv)dxdy - \int_\Omega \nabla(vk\nabla u)dxdy = 0 \tag{d.4}$$

Using divergence theorem for the last term in equation (d.4), we get

$$\int_\Omega \nabla \bullet (vk\nabla u)dxdy = -\int_{d\Omega} vk(\nabla u \bullet n)ds = -\int_{d\Omega} vk\frac{du}{dn}ds \tag{d.5}$$

83

Substituting (d.5) into (d.4), we get

$$\int_{\Omega}(k\nabla u\nabla v + \mu_a uv - fv)dxdy - \int_{\partial\Omega_2} k\frac{du}{dn}vds = 0 \qquad\qquad \text{(d.6)}$$

$$-k\frac{\partial u}{\partial n}v = p(u - \hat{u}) \qquad\qquad \text{(d.7)}$$

Substituting (d.7) into (d.6), we get

$$\int_{\Omega}(k\nabla u\nabla v + \mu_a uv - fv)dxdy + \int_{\partial\Omega_2} p(u - \hat{u})ds = 0 \qquad\qquad \text{(d.8)}$$

The boundary condition on $\partial\phi_1$ is $u = \hat{u}$

The finite element formulation can then be derived from (d.8) as follows

$$\sum K_{ij}u_j = F_j \qquad \text{or} \qquad [K]\{u\} = \{F\}$$

where $K_{ij} = K_{ij}^{(1)} + K_{ij}^{(2)} + K_{ij}^{(3)}$

$$F_i = F_i^{(1)} + F_i^{(2)}$$

$$K_{ij}^{(1)} = \int_{\Omega} k\left(\frac{\partial\phi_i}{\partial x}\frac{\partial\phi_j}{\partial x} + \frac{\partial\phi_i}{\partial y}\frac{\partial\phi_j}{\partial y}\right)dxdy$$

$$K_{ij}^{(2)} = \int_{\Omega} \mu_a\phi_i\phi_j dxdy$$

$$K_{ij}^{(3)} = \int_{\partial\Omega_2} \mu_a\phi_i\phi_j dxdy$$

$$F_i^{(1)} = \int_{\Omega} f\phi_i dxdy$$

$$F_i^{(2)} = \int_{\partial\Omega_2} r\phi_i ds , \quad r = p\hat{u}(s)$$

APPENDIX E

2D POST PROCESSING TOOL

The SIMP method provides solution for material density only at the discrete locations (i.e. elements of FEA model). This presents two major issues: (i) It is difficult to modify the topology with manual interaction and (ii) The topology obtained is not close to being manufacturable. Using a TDF like HRBFN to describe the topology would help circumvent these problems, provided it is easy to manipulate the shape of the HRBFN. An interactive topology modification tool was developed to tweak 2D topologies interactively. The problem formulation can be stated as follows:

Determine HRBFN Parameters to

$$\text{Minimize } f = \sum_{j=1}^{N_e} \left(\rho_j - \rho_{jSIMP} \right)^2 \qquad\qquad \text{(e.1)}$$

where

ρ_j is the density of element j is governed by HRBFN as explained in eq. (7).

ρ_{jSIMP} is the density of element j obtained by SIMP method.

The constraints are bound for HRBFN parameters. Sequential Linear Programming is used to solve this problem. The sensitivity analysis for the objective mentioned in eq. (e.1) is

$$\frac{\partial f}{\partial \hbar} = 2 * \left(\sum_{j=1}^{N_e} \left(\sum_{i=1}^{r} w_i e^{-g_i^2} - \rho_{jSIMP} \right) \right) * \sum_{j=1}^{N_e} \left(\sum_{i=1}^{r} \frac{\partial \left(w_i e^{-g_i^2} \right)}{\partial \hbar_i} \right)$$

(e.2)

where $\hbar_i$ is one of the six parameters for i^{th} basis function.

Fig E.1 (a) shows the maximum natural frequency topology design obtained from SIMP method. Fig E.1 (b) shows the optimal HRBFN parameters computed to fit the SIMP solution. These HRBFN parameters can be further adjusted manually to obtain a manufacturable topology. A post – processing tool was developed for the ease of manual interaction with HRBFN bases and
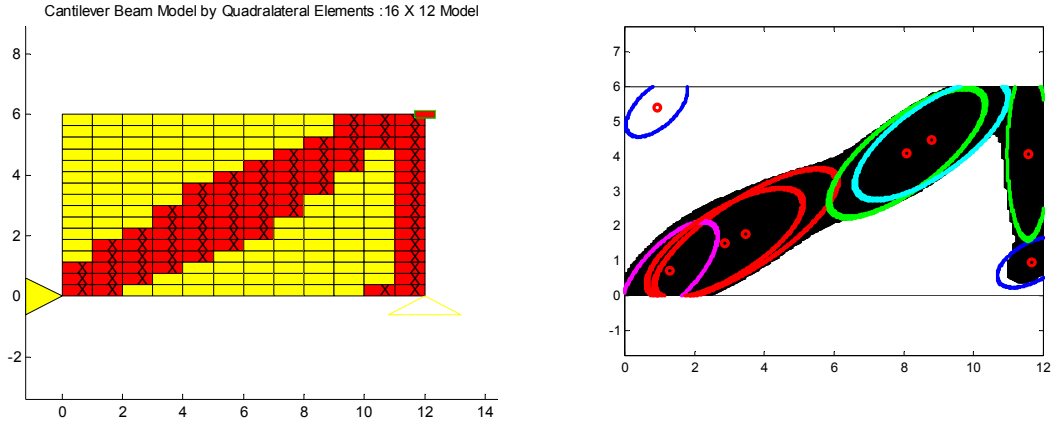
Figure E.1 (a) Topology obtained from SIMP method. (b) HRBFN-Fit for SIMP solution

is described in next section. One of the advantages of HRBFN is that its parameters are intuitive. Hence, it would be easy to make small changes to improve topologies or even design new topologies manually, provided such graphical tool exists. A tool developed to let users interact with 2D HRBFN parameters to perform structural design and modifications is described as follows. Fig E.2 (a) represents the boundary conditions, loading and FEA grid for the example problem. Fig. E.2 (b) shows topology obtained by using HRBFN method as explained in section 3.1 of this work. A bulge at the right end of the structure is visible and clearly looks like an artifact from the optimization solution. This topology is input to the post-processing tool shown in Fig E.3. The tool displays bases in different colors along with their ids, weights and the operation desired. The operations which can be performed on a base are "move", "rotation" and "expansion". "Move" operation lets user drag the base to desired location. "Rotation" operation lets user rotate the base by desired amount. "Expansion" operation lets user expand or contract the base in one of its local x or y dimensions.
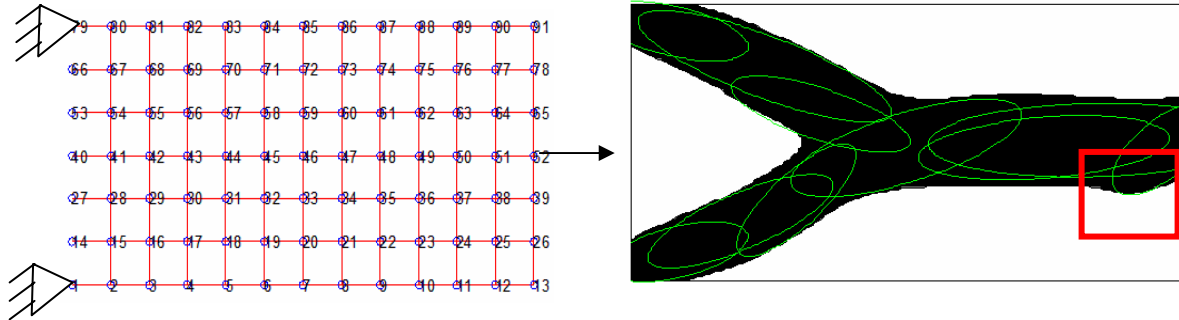
Figure E.2 (a) Boundary conditions, load and FEA grid for compliance minimization example. (b) Topology obtained from SIMP method. Region enclosed by red-rectangle needs tweaking.

Figure E.3 Post-processing tool to design / modify 2-D topologies.

Fig E.4 and E.5 show the modified HRBFN parameters and topology to get rid of bulge observed in Fig E.3. Note that the filtering scheme similar to that described before was used to obtain topology in Fig E.5.

Figure E.4 Modified HRBFN parameters

Figure E.5 Modified topology using post-processing tool

REFERENCES

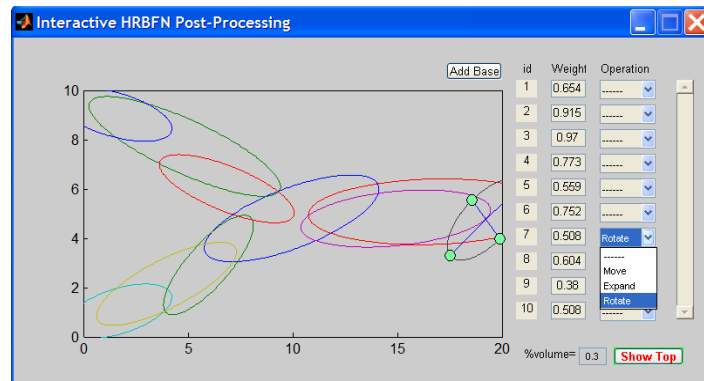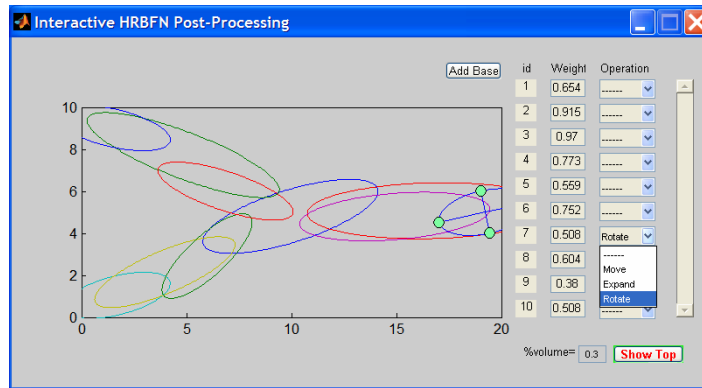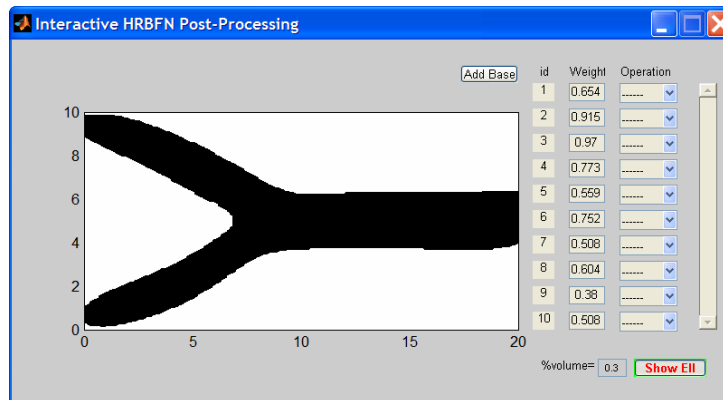[1] Garret N. Vanderplaats, "Structural optimization for statics, dynamics and beyond", Journal of the Brazilian Society of Mechanical Sciences and Engineering, vol.28, no.3, p.316-322, Sept 2006.

[2] Ole Sigmund, Topology optimization: a tool for the tailoring of structures and materials, *Phil. Trans. R. Soc. Lond.* A (2000) 358, 211-227.

[3] G. I. N. Rozvany, "A critical review of established methods of structural topology optimization", Struct Multidisc Optim (2009), Vol. 37, pp. 217–237.

[4] Hans A Eschenauer, Niels Olhoff, "Topology optimization of continuum structures: A review, Appl Mech Rev vol 54, no 4, July 2001.

[5] Kirsh, U, "On singular topologies in optimum structural design", *Structural Optimization*, Vol. 2, No. 3, pp. 133-142, 1990.

[6] Bendsøe, M.P., Kikuchi, N. 1988, "Generating optimal topologies in optimal design using a homogenization method", *Comp. Meth. Appl. Mech. Engrg.*, Vol. 71, No. 2, pp. 197-224, 1988.

[7] Reference: Fatma Y. Kocer, Colby C. Swan, Jasbir S. Arora, "Comparison of Continuum and Ground Structure Topology Optimization Methods for Concept Design of Structures", ASCE Structures Congress April 19−21, 1999, New Orleans, LA.

[8] Bendsøe M.P., "Optimal shape design as a material distribution problem", *Struct. Multidisc. Optim.*, Vol. 1, No. 4, pp. 193–202, 1989.

[9] M. Stolpe and K. Svanberg, "An alternative interpolation scheme for minimum compliance topology optimization", *Struct Multidisc. Optim*, Vol. 22, No. 2, pp. 116–124, 2001

90

[10] V. Kumar, M.D. German, G. J. Lee, "A geometry-based 2-dimensional shape optimization methodology and a software system with applications", *Proceedings of the 3rd International Conference on CAD/CAM Robotics and Factories of the Future*, Vol. 2, Springer, New York, 1", pp. 5-10, 1989.

[11] P.M. Finnigan, A. Kela, J. E. Davis, "Geometry as a basis for finite element automation", *Engineering with Computers*, Vol. 5, No. 5, pp. 147-160, 1989.

[12] De Ruiter, M.J. and Van Keulen, F., "Topology Optimization: approaching the material distribution problem using a topological function description", *Struct. Multidisc. Optim.*, Vol. 26, No 6, pp. 406–416, 2004.

[13] S.Y. Wang, K.M. Lim, B.C. Khoo, M.Y. Wang, "An extended level set method for shape and topology optimization", *Journal of Computational Physics*, Vol. 221, No. 1, pp. 395–421, 2007.

[14] Thomas A. Poulsen, "Topology optimization in wavelet space", *Int. J. Numer. Meth. Engng*, Vol. 53, No. 3, pp. 567–582, 2002.

[15] W. Annicchiarico, M. Cerrolaza, "Finite elements, genetic algorithms and β- splines: a combined technique for shape optimization", *Finite Elements in Analysis and Design*, Vol. 29, No. 3-4, pp. 231-257, 1998.

[16] Cui GY, Tai K, Wang BP, Topology optimization for maximum natural frequency using simulated annealing and morphological representation, *AIAA Journal*, Vol. 40, No. 3, pp. 586–589, 2002.

[17] Poggio, Tomaso and Girosi, Federico, "A Theory of Networks for Approximation and Learning", *A.I. Memo*, No. 1140, C.B.I.P. Paper No. 31, July 1989.

[18] Poggio, Tomaso and Girosi, Federico, "Network for approximation and learning", *Proc. IEEE*, vol. 78, No. 9, pp. 1481-1496, 1990.

[19] Chyi-Yeu Lin and Fang-Ming Hsu, "An adaptive volume constraint algorithm for topology optimization with a displacement-limit", *Advances in Engineering Software*, Vol. 39, Issue 12, pp. 973-994, Dec 2008.

[20] Lyness,J.N. and C.B. Moler, "Numerical differentiation of analytical functions", *SIAM J. Numer. Anal.*, Vol.4, pp.202-210, 1967.

[21] B. P. Wang and A. Apte, "Complex variable method for eigensolution sensitivity analysis", *American Institute of Aeronautics and Astronautics Journal*, Vol. 44, Issue 12, pp. 2958-2961, 2006.

[22] Kennedy, J. Eberhart, R., "Particle Swarm Optimization", Proceedings of IEEE International Conference on Neural Networks, Vol. 4, pp. 1942-1948, Nov/Dec 1995.

[23] Manoj Tayal, "Particle Swarm Optimization for Mechanical Design", Master's Thesis, University of Texas at Arlington, 2003.

[24] Garret N. Vanderplaats, "Numerical Optimization Techniques for Engineering Design: with Applications", Mcgraw-Hill College, New York, Feb. 1984.

[25] Sigmund, O., "A 99 line topology optimization code written in Matlab", Structural and Multidisciplinary Optimization. Vol. 21, pp.120-127, 2001.

[26] D. Tcherniak and O. Sigmund, A web-based topology optimization program, *Structural and Multidisciplinary Optimization*, Vol. 22, Issue 3, pp. 179-187, 2001.

[27] Atsushi Koguchi, Noboru Kikuchi, "A surface reconstruction algorithm for topology optimization", *Engineering with Computers*, Vol. 22, Issue 1, pp. 1-10, 2006.

[28] A. V. Kumar and D. C. Gossard, "Synthesis of Optimal Shape and Topology of Structures," *ASME, J. Mech. Des.*, 118, pp. 68-74, 1996.

[29] Ming-Hsiu Hsu, Yeh-Liang Hsu, "Interpreting three-dimensional structural topology optimization results", *Computers & structures*, Vol. 83, Issue 4-5, pp. 327-337, 2005.

92

[30] J O Deasy, A I Blanco and V H Clark, "CERR: a computational environment for radiotherapy research", *Medical Physics.,* Vol. 30, Issue 5, pp. 979–985, 2003.

[31] R. Myerson, M. Garofalo, I. El Naqa, R. Abrams, A. Apte, W. Bosch, P. Das, L. Gunderson, T. Hong, J. Kim, "Elective Clinical Target Volumes for Conformal Therapy in Anorectal Cancer: A Radiation Therapy Oncology Group Consensus Panel Contouring Atlas"**,** *International Journal of Radiation OncologyBiologyPhysics* , Vol. 74 , No. 3, pp. 824-830, July 2009.

[32] Sigmund Ole (1997) On the Design of Compliant Mechanisms Using Topology Optimization. Mechanics Based Design of Structures and Machines, 25 (4), 493–524.

[33] Frecker M. I., Ananthasuresh G. K., Nishiwaki S., Kikuchi N., Kota S. (1997) Topological synthesis of compliant mechanisms using multi-criteria optimization. Journal of Mechanical Design, 119 (2), 238-245.

 [34] Frecker M., Kikuchi N., Kota S. (1999) Topology optimization of compliant mechanisms with multiple outputs. Structural and Multidisciplinary Optimization 17 (4), 269-278.

[35] Nishiwaki Shinji, Frecker M. I., Min Seungjae, Kikuchi N. (1998) Topology optimization of compliant mechanisms using the homogenization method. International Journal of Numerical Methods in Engineering, 42 (3), 535-559.

[36] Arora Jasbir S. (1976) Survey of Structural Reanalysis Techniques, Journal of the Structural Division 102 (4), 783-802.

[37] Chen Suhuan, Huang Cheng, Liu Zhongsheng (1999) Static Reanalysis for Topological Modifications of Structures. Acta Mechanica Solica Sinica 12 (2), 155-164.

[38] Kirsch U. (1993) Efficient reanalysis for topological optimization, Structural Optimization 6, 143-150, 1993.

[39] Kirsch U., Liu S. H. (1997) Structural reanalysis for general layout modifications. AIAA Journal 35 (2), 382-388.

[40] S. R. Arridge, "Optical tomography in medical imaging", *Inverse Problems*, Vol. 15, 1999.

[41] V. Kolehmainen, S. R. Arridge, M. Vauhkonen and J. P. Kaipio, "Simultaneous reconstruction of internal tissue region boundaries and coefficients in optical diffusion tomography", Physics in Medicine and Biology, June 22, 2000.

[42] H. Liu, Y. Song, K. L. Worden, X. Jiang, A. Constantinescu, and R. P. Mason, "Noninvasive investigation of blood oxygenation dynamics of tumors by near infrared spectroscopy", Applied optics, Vol. 39, No. 28, 2000.

[43] Jun Zhou, Jing Bai and Ping He, "Spatial location weighted optimization scheme for DC optical tomography", Optical Express, Vol. 11, No. 2, Jan 27, 2003.

[44] S. R. Arridge, M. Hiraoka and D. T. Delpy, "Finite element method for the propogation of light in scattering media: boundary and source conditions", Medical Physics, Vol. 22, Issue 11, 1995.

[45] S. R. Arridge and J. C. Hebden, "Optical imaging in medicine: II Modeling and reconstruction", Phys. Med. Biol. vol. 42, 1997.

[46] S. R. Arridge, "Optical tomography in medical imaging", Inverse Problems, Vol. 15, 1999.

[47] Martin Schweiger, Leonid Zhukov, Simon R. Arridge and Cristopher R. Johnson, "Optical tomography using the SCIRun problem solving environment: Preliminary results for three-dimensional geometries and parallel processing", Optics Express, Vol. 4, No. 8, April 12, 1999.

[48] M. V. Klibonov, T. R. Lacu and R. M. Frank, "A fast and accurate algorithm in optical/ diffusion tomography", Inverse Problems, April 11, 1997.

[49] B. W. Pogue, S. Geimer, T. O. McBride, S. Jiang, U. L. Osterberg and K. D. Paulsen, "Three-dimensional simulation of near-infrared diffusion in tissue: boundary condition and geometry analysis for finite-element image reconstruction", Applied Optics, Vol. 40, no. 4, Feb 2001

[50] H. Dehghani, B. Brooksby, K. Vishwanath, B. W. Pogue, and K. D. Paulsen, "The effects of internal refractive index variation in near infrared optical tomography: a finite element modeling approach", Phys. Med Biol, Vol 48, 2003

[51] Yong Xu, Xuejun Gu, Taufiquar Khan and Haubei Jiang, "Absorption and scattering images of heterogeneous scattering media can be simultaneously reconstructed by use of dc data", Applied Optics, Sept 1, 2002

[52] A. H. Hielscher, A. D. Klose, and K. M. Hanson, "Gradient-based iterative image reconstruction scheme for time resolved optical tomography", IEEE Transaction on Medical Imaging, Vol. 18, no. 3, March 1999.

[53] Haubei Jiang, "Optical image reconstruction based on the third order diffusion equations", Optics Express, Vol. 4, No. 8, April 12, 1999.

[54] Taufiquar Khan and Haubei Jiang, "A new diffusion approximation to the radiative transfer equation for scattering media with spatially varying refractive indices, Journal of Optics, Feb 14, 2003.

BIOGRAPHICAL INFORMATION

Aditya Prakash Apte obtained Master's degree in Mechanical Engineering from the University of Texas at Arlington. Currently he works at Washington University Medical School in Saint Louis, MO as Bioinformaticist in the department of Radiation Oncology. His interests include simulation based design and software development.